**Astronomy
&
Astrophysics**

Diagnostics of the molecular component of photon-dominated regions with mechanical heating[*]

M. V. Kazandjian[1], R. Meijerink[1,2], I. Pelupessy[1], F. P. Israel[1], and M. Spaans[2]

[1] Sterrewacht Leiden, PO Box 9513, 2300 RA Leiden, The Netherlands
e-mail: mher@strw.leidenuniv.nl
[2] Kapteyn Astronomical Institute, PO Box 800, 9700 AV Groningen, The Netherlands

ABSTRACT

Context. Multitransition CO observations of galaxy centers have revealed that significant fractions of the dense circumnuclear gas have high kinetic temperatures, which are hard to explain by pure photon excitation, but may be caused by dissipation of turbulent energy.
Aims. We aim to determine to what extent mechanical heating should be taken into account while modeling PDRs. To this end, the effect of dissipated turbulence on the thermal and chemical properties of PDRs is explored.
Methods. Clouds are modeled as 1D semi-infinite slabs whose thermal and chemical equilibrium is solved for using the Leiden PDR-XDR code, where mechanical heating is added as a constant term throughout the cloud. An extensive parameter space in hydrogen gas density, FUV radiation field and mechanical heating rate is considered, covering almost all possible cases for the ISM relevant to the conditions that are encountered in galaxies. Effects of mechanical heating on the temperature profiles, column densities of CO and H_2O and column density ratios of HNC, HCN and HCO^+ are discussed.
Results. In a *steady-state* treatment, mechanical heating seems to play an important role in determining the kinetic temperature of the gas in molecular clouds. Particularly in high-energy environments such as starburst galaxies and galaxy centers, model gas temperatures are underestimated by at least a factor of two if mechanical heating is ignored. The models also show that CO, HCN and H_2O column densities increase as a function of mechanical heating. The HNC/HCN integrated column density ratio shows a decrease by a factor of at least two in high density regions with $n \sim 10^5$ cm^{-3}, whereas that of HCN/HCO^+ shows a strong dependence on mechanical heating for this same density range, with boosts of up to three orders of magnitude.
Conclusions. The effects of mechanical heating cannot be ignored in studies of the molecular gas excitation whenever the ratio of the star formation rate to the gas density ($SFR/n^{3/2}$) is close to, or exceeds, 7×10^{-6} $M_\odot$ yr^{-1} cm$^{4.5}$. If mechanical heating is not included, predicted column densities (such as those of CO) are underestimated, sometimes (as in the case of HCN and HCO^+) even by a few orders of magnitude. As a lower bound to its importance, we determined that it has non-negligible effects already when mechanical heating is as little as 1% of the UV heating in a PDR.

Key words. galaxies: ISM – photon-dominated region (PDR)

1. Introduction

Radiation originating from the molecular gas in various galaxy environments, including galaxy centers, provides information about the physical state of these environments such as the gas mass and temperature, or the source of its excitation. The far-ultraviolet radiation (FUV; $6.0 < E < 13.6$ eV) emitted by newly formed luminous stars and X-rays ($E > 1$ keV) produced by black hole accretion have very distinct effects on the thermo-chemical balance of the gas. Strong FUV illumination results in so-called photon-dominated regions (PDRs; Tielens & Hollenbach 1985), while X-ray irradiation creates X-ray dominated regions (XDRs; Maloney et al. 1996). In PDRs and XDRs, the thermal and chemical structure is completely determined by the radiation field, and directly reflects the energy balance of the interstellar gas. For example, in PDRs the CO is generally much cooler ($T \sim 10-30$ K) than in XDRs ($T \sim 20-500$ K), therefore XDRs generally exhibit CO emissions to much higher J levels. Thus, observations of the CO ladder allow us to discriminate between the different types of radiation fields.

Recently, it has become clear that PDR and XDR excitation is not sufficient to fully explain observed molecular line emission ratios. For instance, Loenen et al. (2008) have found that the HCN, HNC, and HCO^+ line ratios observed towards (ultra-)luminous infrared galaxies span a parameter space that cannot be reproduced by models in which FUV or X-ray radiation dominates. In their study they showed that an additional heating mechanism is required, which they suggest to be mechanical heating caused by dissipating supernova shocks, injected on large scales and cascading down through turbulent dissipation to the smallest scales. More recently, Papadopoulos (2010) has suggested that cosmic ray ionization rates in such galaxies may exceed those measured in the Milky Way by factors of 10^3 to 10^4, hence significantly affect the ionization balance and thermal-chemical structure of interstellar clouds. The effects of high cosmic ray rates on ISM chemistry is studied in detail by Meijerink et al. (2011) (who consider mechanical heating as well only for selected models) and Bayet et al. (2011).

However, neither the models by Loenen et al. (2008) nor those by Meijerink et al. (2011) treat mechanical heating self-consistently, as it is only implemented as an additional heating term and not as feedback from hydrodynamics. The dynamical

---

[*] Appendix A is available in electronic form at
http://www.aanda.org

evolution of the interstellar medium in galaxies in general and close to a super-massive black hole in particular, has been studied in 3D hydrodynamic simulations (Wada & Norman 2002; Wada & Tomisaka 2005) but these in turn lacked chemistry, and line emission maps of the various molecules were created by using constant abundances. A study by Pérez-Beaupuits et al. (2011) improved on this by using chemical abundances obtained from the Meijerink & Spaans (2005) XDR code. Nevertheless, these simulations still lack UV input and feedback from the hydrodynamics on the chemistry still needs to be done self-consistently.

The dominant coolants in the ISM which are commonly observed are the [CI] 609 μm, [CII] 158 μm and the [OI] 63 μm lines. These fine-structure lines are not sensitive to additional mechanical heating, when the clouds are already illuminated by FUV radiation Meijerink et al. (2011). This is in contrast to the molecular species that are formed in regions of the cloud, that are shielded from irradiation. Thus in this paper we consider molecular species as possible candidates for tracing regions which are dominated by mechanical heating. Although a simple dust model is taken into account (Meijerink & Spaans 2005), dust diagnostics are not discussed since these diagnostics are out of the scope of this paper. We will explore the possible tracers in a number of steps. In this paper, we will first establish under which physical conditions mechanical heating is important. We will estimate what range of mechanical heating rates we may expect for the different densities in the ISM. We will then determine how this affects the thermo-chemical balance in the models, and, by way of first application, discuss the effect on the integrated column densities of common molecular species such as CO, H_2O, HNC, HCN and HCO^+, and some of their ratios. In subsequent papers, we will calculate line emission maps that can be compared directly to the detailed observations obtained with (sub)millimeter telescopes, notably the Atacama Large Millimeter Array. Ultimately, our aim is to couple chemistry and hydrodynamics in order to treat the relevant physical effects in a self-consistent manner.

2. Methods

We solve the equilibrium state of all model clouds by using an optimized version[1] of the Leiden PDR-XDR code developed by Meijerink & Spaans (2005) (Details of the optimization and further improvements are mentioned in Sect. 2.2). In its present form, the code assumes a 1D PDR geometry where various heating and cooling processes are included in solving for the thermal and chemical balance. The radiative transfer for the cooling lines and the escape probabilities are computed based on the work by de Jong et al. (1980). We refer the reader to Meijerink & Spaans (2005) for further details on the thermal processes and chemical network used in solving for the steady state equilibria.

2.1. Parameter space and reference models

In order to reduce the number of free parameters, we considered three metallicity levels, the benchmark being $Z = Z_\odot$ (solar metallicity) to which we added $Z = 0.5 \, Z_\odot$ (characteristic of moderately metal-poor dwarf galaxies) and $Z = 2 \, Z_\odot$ (characteristic of spiral galaxy center conditions). Throughout the paper, our discussion concentrates on the $Z = Z_\odot$ models[2]. For the

---

[1] The optimized code is called PDR-XDR-1.1.
[2] The analogous grids for the other two metallicities are presented in Appendix A.

cosmic-ray ionization rate, we adopted the value 5×10^{-17} s^{-1} used in Meijerink & Spaans (2005) which is close to that in the solar neighborhood. The grids consisted of models spanning a wide range of physical conditions, uniformly sampled (in $\log_{10}$ scale) in ambient gas density $1 < n < 10^6$ cm^{-3}, incident radiation field $0.32 < G_0 < 10^6$ and mechanical heating $10^{-24} < \Gamma_{mech} < 10^{-16}$ erg cm^{-3} s^{-1}. In the absence of mechanical heating, n and G_0 dominate the characteristics of a PDR. The ambient gas density n is the total number density of hydrogen nuclei, which is set constant throughout the slab. The values considered cover the full range of densities encountered in the diffuse interstellar medium to those of dense molecular cloud cores. The incident FUV radiation field G_0 is measured in so-called Habing units (Habing 1969) corresponding to 1.6×10^{-3} erg cm^{-2} s^{-1}. The values considered here include radiation fields ranging from only a few times stronger than the relatively low solar neighborhood field to the intense fields irradiating clouds close to young OB associations; the upper limit corresponds to the radiation field intensity at a distance of about 0.1 pc from an O star.

In constraining a physically relevant range of mechanical heating rates, we took a combination of values recovered from softened particle hydrodynamics simulations (SPH hereafter) (Pelupessy 2005), and added estimates of mechanical heating rates induced by turbulence caused by supernova shocks that are dissipated in the ISM (Loenen et al. 2008). The SPH simulations are of dwarf galaxies with n up to $\sim 10^3$ cm^{-3} where the mechanical heating rates ranged from $\sim 10^{-30}$ to 10^{-22} erg cm^{-3} s^{-1} for such densities. When naively extrapolated to densities of 10^6 cm^{-3}, rates up to 10^{-18} erg cm^{-3} s^{-1} are expected. In the Loenen et al. (2008) recipe, it is assumed that $\eta = 10\%$ of the supernova blast energy ($E_0 = 10^{51}$ erg per SN event) is absorbed throughout the continuous starburst region (a region which by definition sustains a considerably high SFR, which is steady, by consuming the available gas), whose size is taken to be $D_{SB} = 100$ pc. Equation (1), which is a combination of Eqs. (3) and (4) in Loenen et al. (2008), relates Γ_{mech} to the the supernova rate (SNR),

$$\Gamma_{mech} = \frac{SNR E_0 \eta}{V_{SB} V_{PDR} n_{PDR}} \tag{1}$$

where V_{SB} is the volume of the starburst region, whereas V_{PDR} and n_{PDR} are the volume and number density of PDRs in that starburst region respectively. They also assumed that the absorbed energy is distributed evenly among the PDRs in this starburst region. The number of the PDRs in the starburst region is estimated by assuming a gas density contrast of 10 (the inverse of the filling factor) between that of the PDRs and the ambient ISM of the starburst. Considering a Salpeter IMF for the stellar population, the star formation rate (SFR) is related to the SNR via $SNR/SFR = 0.0064$ (see Dahlén & Fransson 1999, for details). In computing the SNR, they assumed that stars with $M > 8 \, M_\odot$ end up as supernovae (see Loenen et al. 2008, for more details on the estimates and assumptions). A Kroupa (2001) IMF, over the mass range from 0.1 $M_\odot$ to 125 $M_\odot$ considered, would result in a marginally higher $SNR/SFR \sim 0.01$. This higher rate reflects a slightly enhanced mechanical heating rate. However, the difference in the resulting Γ_{mech} between both IMFs over the same mass range is $\sim 40\%$, thus for simplicity we adopted the Salpeter IMF.

By way of example, a mechanical heating rate Γ_{mech} of 2×10^{-20} erg cm^{-3} s^{-1} is expected in a quiescent disk, such as that of the Milky Way with an $SFR \sim 1 \, M_\odot$ yr^{-1} and an SNR of ~ 0.01 yr^{-1}. In regions with active star formation

Table 1. Parameters of the reference models.

Model name	$\log n$ (cm^{-3})	$\log G_0$
M1	3.0	3.0
M2	3.0	5.0
M3	5.5	3.0
M4	5.5	5.0

Notes. These are identical to the ones in Meijerink & Spaans (2005). M1 and M2 correspond to low density clouds in galactic centers in the presence of a starburst event, whereas M3 and M4 correspond to much denser clouds where excitation of high density gas tracers such as HCN is possible.

($SFR \sim 50\ M_\odot$ yr^{-1} and $SNR \sim 0.3$ yr^{-1}) the mechanical heating rate is much higher, $\Gamma_{\text{mech}} = 1 \times 10^{-18}$ erg cm^{-3} s^{-1}. For extreme starbursts with ($SFR \sim 1000\ M_\odot$ yr^{-1} and $SNR \sim 6.4$ yr^{-1}) mechanical heating rates $\Gamma_{\text{mech}} = 2 \times 10^{-17}$ erg cm^{-3} s^{-1} are possible. Another source of mechanical energy input is the outflows of young stellar objects (YSOs). The outflow phase is short-lived, and as discussed by (Loenen et al. 2008) a nearby dense cloud ($n > 10^5$ cm^{-3}) is required for a significant amount of energy to be absorbed by the surrounding ISM (compared to the mechanical heating due to supernovae). Hence energy input due to YSOs is ignored in this study. Based on a similar order of magnitude estimate, mechanical energy input due to stellar winds are also ignored, since they would contribute up to 6% to the total mechanical heating (Pelupessy 2005; Leitherer et al. 1999).

It is of interest to determine the effects of mechanical heating by comparing the results obtained from models with and without a mechanical heating term. To this end, we have selected from the grids calculated for analysis and discussion in this paper the same reference models that were studied in detail by Meijerink & Spaans (2005) without taking into account mechanical heating. These models are summarized in Table 1.

In this first exploration, Γ_{mech} is added per unit volume. In doing so for a certain grid, each model in the $n - G_0$ parameter space has an extra Γ_{mech} added to its heating budget. Another choice could have been the addition of Γ_{mech} per unit mass, where for a certain grid the amount of added mechanical heating would be proportional to the gas density of the model in the grid. For simplicity we considered adding mechanical heating per unit volume.

2.2. Numerical schemes

Finding the thermal and chemical equilibrium for each slab is an $(N+1)$-dimensional numerical root finding problem. N being the number of species (atomic and molecular species and electrons) in the chemical network in addition to the thermal balance. It involves solving the set of non-linear equations Eqs. (2) and (3),

$$\mathrm{d}\boldsymbol{n}(T)/\mathrm{d}t = 0 \tag{2}$$

$$\Gamma(T, \boldsymbol{n}) - \Lambda(T, \boldsymbol{n}, t) = 0. \tag{3}$$

The first equation (chemical balance) is the rate of change of the density of the species at a certain temperature T. We solved for this vector equation of length N following the recipe by Tielens & Hagen (1982) in using the multi-dimensional Newton-Raphson method. The thermal balance is solved for in the second equation, where Γ and Λ are the total heating and cooling rates. These two terms are a 1D function of $\boldsymbol{n}$ (used as input from the previous equation) and T. This process is repeated

iteratively until convergence with a tolerance of 10^{-6} for the chemical balance and 10^{-3} for the thermal balance. Two major improvements lead to a speed-up by a factor of $\sim$30 over the original PDR-XDR code. These are (a) tweaking the LU decomposition (optimizing compiler flags and matrix elements storage scheme) used in the multi-dimensional Newton-Raphson root finding; and (b) using in the thermal balance root finding the secant method (with a convergence order of $\sim$1.6) instead of the bisection method which has a linear convergence rate.

The distance from the surface of the cloud is measured in terms of the visual extinction (A_V) due to interstellar dust. It is related to the total column density of hydrogen nuclei N(H) according to Eq. (4) (Bohlin et al. 1978),

$$A_V = 5.34 \times 10^{-22}\ N_H\ Z\ \text{mag cm}^{-2}. \tag{4}$$

Once the equilibrium state of the surface slab (with zero thickness) is solved for, the width of the remaining slabs is chosen adaptively while resolving the transition zone which has large temperature gradients compared to the small temperature gradients at the surface of the slab and at high depths. This is also one of the changes over the original implementation. In choosing the slab width adaptively, the maximum allowed relative difference in the temperature between consecutive slabs was set to 5%. Smaller values were tested as well, where no significant difference was noticed.

It is assumed that the mechanical heating due to turbulence is absorbed by the ISM at all scales. Hence for simplicity Γ_{mech} is added *uniformly* throughout the cloud.

Molecular clouds may have a visual extinction up to 200 mag (Tielens & Hagen 1982). Beyond $A_V \sim 5$ mag most of the species become molecular whereas for $A_V > 10$ mag all abundances are almost constant since physical conditions do not change anymore. The maximum depth, we allowed for, in all the models, was $A_V = 20$ mag. This corresponds to N(H) $= 7.5 \times 10^{22}, 3.7 \times 10^{22}$ and 1.8×10^{22} cm^{-2} for metallicities of $Z = 0.5$, 1 and 2 $Z_\odot$ respectively. This enables us to compare clouds of different metallicities up to the same column density. In doing so, a fixed N(H) $= 1.8 \times 10^{22}$ cm^{-2} (the maximum N(H) for $Z = 2\ Z_\odot$) was adopted in the illustrations where column densities of molecular species were used.

For each value of mechanical heating and metallicity, 25×25 models equally spaced in $\log_{10} n$ and $\log_{10} G_0$ were calculated, up to a total of $\sim$16 000 models. When there is no or very little mechanical heating, the temperature may drop below 10 K at a certain depth in the cloud. Since the code is designed to work for $10 < T < 10^4$ K[3], for slab elements where the lower limit is reached we solved the chemical network for a fixed temperature of 10 K. In making the convergence more robust, we built a small database of guess values (used as input in the root finding) for the surface slab. This enabled us to explore regions in the parameters where the original implementation failed.

In running the models, an improved version of the PDR-XDR code was incorporated into the Astrophysical Multipurpose Software Environment (AMUSE) framework. The

---

[3] The lower bound in the temperature is set to 10 K since many reaction constants become inaccurate below that value (Röllig 2011). He and Fe$^+$ cooling become important above 10^4 K which make the thermal balance inaccurate since these are not included in the current version (in addition to other dielectronic recombination processes). But below 10^4 K, the contribution of these processes is negligible to the total cooling. Also for $T > 10^4$ K, the heating efficiency expression becomes inaccurate. However, not many models exceed 10^4 K, but we allowed that since it is needed to make the models converge as the solution is progressed into the cloud.
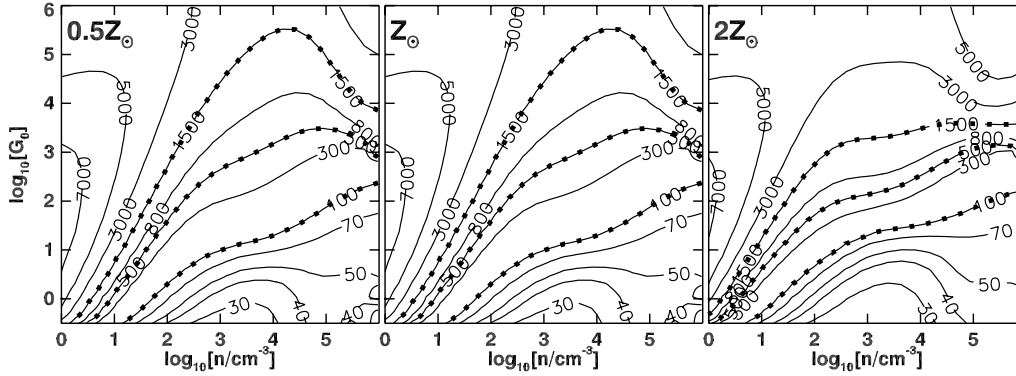
Fig. 1. Temperature profile (without mechanical heating) at the cloud surface for different metallicities. Generally, the temperature rises as a function of G_0 and constant n, since the dominant heating term is the photo-electric heating, which is proportional to G_0. However the behavior for constant G_0 as a function of n is not as trivial. See Sect. 3.1 of Kaufman et al. (1999) and Sect. 3 of Meijerink et al. (2007) for more discussion of the topology of the contours. This version of the code covers a larger parameter range than Meijerink et al. (2007). Solid lines with filled squares highlight the temperature contours for 100, 500 and 1500 K. The most significant change when comparing the three panels is for the 1500 K contour, where for $Z = 2\,Z_\odot$ higher temperatures are attained (compared to the lower metallicities) in the same part of the parameter space ($n > 10^3$ cm^{-3}, $G_0 > 10^4$).

AMUSE package allows astrophysical codes from different domains to be combined to conduct numerical experiments (see Pelupessy & Portegies Zwart 2012, for a more complete description). It is a development of the Multi-physics and Multi-scale Software Environment (MUSE, Portegies Zwart et al. 2009) and is freely available for download[4]. (The PDR code itself will be made available in the future.) The interface to the Meijerink PDR-XDR code takes the main parameters G_0, n, $\Gamma_{\rm mech}$ as input and calculates the PDR equilibrium properties. This will allow the code to eventually be used as an equilibrium sub-grid model for e.g. galaxy scaled hydrodynamic simulations. In the present work this feature is not used, only the capability to run many models in parallel is.

3. Results

In this section we present the comparisons for thermal and chemical diagnostics of the grids modeled with and without mechanical heating. We start by discussing the temperatures at the cloud surface, and at the maximum cloud depth considered since for a given model, the gas temperature to a large extent determines the chemical composition. Following this, we will discuss the statistical properties of the CO, H_2O, HCN, HNC and HCO^+ molecules which are important diagnostics for moderate and dense gas. Throughout this section, we use the reference models (M1 to M4) to illustrate the impact of mechanical heating on the properties of the PDRs as a function of depth.

3.1. Gas temperature

In the absence of other heating terms (such as due to mechanical heating) PDRs are characterized by rapid decreases in temperature, from ~1000 K at the surface down to ~10 K in regions where A_V exceeds 10 mag. Since mechanical heating may be expected to considerably change the temperature structure, we will first explore this.

3.1.1. Temperature at the surface

At the surface we only need to solve for the equilibrium of a single slab (with zero thickness). Because this can be done much

faster than in the case of a full slab, a higher resolution is possible for the surface grids. These surface grids therefore consisted of 2500 (50×50) models uniformly sampled in $\log_{10} n$ and $\log_{10} G_0$. In Fig. 1 the surface temperature, without mechanical heating ($\Gamma_{\rm mech} = 0$ erg cm^{-3} s^{-1}), is shown for three different metallicities. The temperature contours are in good agreement with the profiles recovered by Kaufman et al. (1999) and Meijerink et al. (2007)(which uses the original implementation). We note that metallicity has little effect on the overall topology of the contour plots, except for regions where $G_0 > 10^4$, especially where $n > 10^4$ cm^{-3}. The temperature almost doubles as Z is increased from $Z_\odot$ to $2\,Z_\odot$, with no noticeable change between $Z = 0.5\,Z_\odot$ and $Z = Z_\odot$. This is because cooling scales as Z whereas the dominant heating term scales almost as Z for low n but increases to $\sim Z^2$ as n increases to 10^6 cm^{-3}. This temperature dependence on metallicity has also been observed by Röllig et al. (2006). It is worth noting that in the lower right-hand corner of the grid ($n > 10^{5.5}$ cm^{-3}, $G_0 < 5$) three equilibria were found, one unstable and two stable ones. The stable equilibria correspond to a low (~50 K) and a high temperature (~300 K) state with the unstable one in-between. Here we have shown the low-temperature equilibrium. In any case, we note that this part of the parameter space is not of physical relevance for systems that interest us here.

The dominant heating term at the cloud surface is photo-electric heating, where electrons ejected from the dust grains collide elastically with the gas and heat it. The typical efficiency (ϵ) of this process is quite low 0.5 to 1% with a maximum of ~5% (Black & Dalgarno 1977). The photo-electric heating rate ($\Gamma_{\rm photo}$) at the surface is given by the expression (Bakes & Tielens 1994):

$$\Gamma_{\rm photo} = 10^{-24} \epsilon G_0 n \ {\rm erg \ cm^{-3} \ s^{-1}} \tag{5}$$

where ϵ depends on electron density ($n_{\rm e}$), G_0 and gas temperature. The expression for ϵ is given in Eq. (6) (Bakes & Tielens 1994),

$$\epsilon = \frac{4.87 \times 10^{-2}}{1 + 4 \times 10^{-3} \left(G_0 T^{1/2}/n_{\rm e}\right)^{0.73}} + \frac{3.65 \times 10^{-2} \left(T/10^4\right)^{0.7}}{1 + 2 \times 10^{-4} \left(G_0 T^{1/2}/n_{\rm e}\right)} \tag{6}$$

hence the $\log_{10}$ of Eq. (5) is linear in $\log_{10} n$ and $\log_{10} G_0$ whenever ϵ is constant. Figure 2 shows the total heating in the
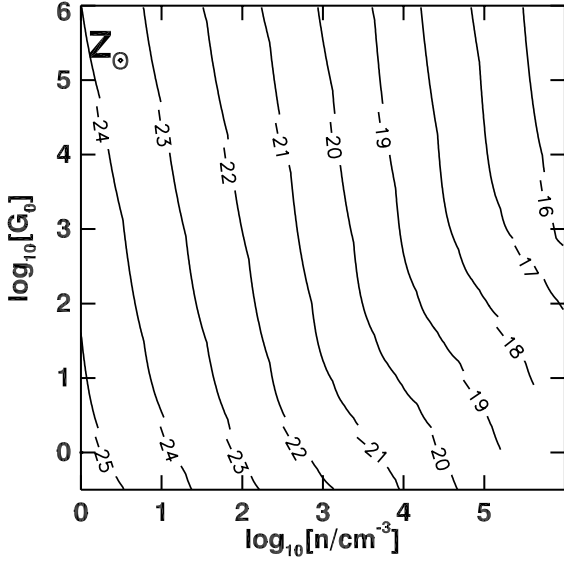
Fig. 2. Total heating at the cloud surface without mechanical heating. The main characteristic of this plot is that above the diagonal, the contours are parallel straight lines; whereas below the diagonal ($G_0 = n$ line), there is a break in the slope, indicating that photo-electric heating is no longer the dominant mechanism in that region. The minimum total heating is on the order of $10^{-25.5}$ erg cm^{-3} s^{-1} at the lower left corner and $10^{-15.2}$ erg cm^{-3} s^{-1} at the top right corner.

$n - G_0$ plane. In the top part of the plot, the contours are almost straight lines. This is not surprising, Γ_{photo} accounts in most cases for more than 95% of the total heating budget. To illustrate this, we look at the logarithm of Eq. (5), which in expanded form becomes:

$$\log_{10} \Gamma_{photo} = -24 + \log_{10} \epsilon + \log_{10} G_0 + \log_{10} n \qquad (7)$$

which is linear in both $\log_{10} G_0$ and $\log_{10} n$. This means that the heating efficiency is almost constant wherever the contours are straight lines. This is not true in the regions below the break in the contour lines which occurs in the region under the $G_0 = n$ line in Fig. 2. In that part of parameter space, photo-electric heating is complemented by H$_2$ photo-dissociation heating. However, this is a small part of the total parameter space, so that we are justified in using photo-electric heating as a good approximation for the total heating. Hence, we expect total heating to have a linear dependence on $\log_{10} n$ for constant values of G_0. This is achieved by fitting horizontal cuts of Γ_{total} in Fig. 2 as a function of n for different values of G_0.

From the fits, we could see that the minimum surface heating for the lowest density gas considered ($n = 1$ cm^{-3}) ranges from $10^{-25.6}$ erg cm^{-3} s^{-1} (for low G_0) to $10^{-24.0}$ erg cm^{-3} s^{-1} (for high G_0). In contrast, the maximum surface heating for $n = 10^6$ cm^{-3}, is $10^{-15.2}$ erg cm^{-3} s^{-1}. We also observe that the surface heating scales as $n^{1.21}$ for $G_0 < 10^2$ and $n^{1.55}$ for $G_0 > 10^4$.

The equilibrium temperature is expected to vary depending on the amount of extra heating introduced via Γ_{mech}. Following this simple assumption, we expect to have significant changes in the equilibrium temperature when Γ_{mech} is comparable to the total surface heating, with a varying impact on different parts of the parameter space. In order to determine the zone in the parameter space where Γ_{mech} alters the equilibrium state, we solve for n in Eq. (7) by equating it to Γ_{mech}. In other words, we solve for n in $\Gamma_{total,surface}(n) = \Gamma_{mech}$ for the range in Γ_{mech} we have considered in our parameter space. These solutions, n_c, listed in

Table 2. Estimated values of gas density, where clouds with lower densities (listed in the bottom row), the shape and equilibrium temperature of the contours of Fig. 1 are significantly effected by Γ_{mech} (top row). For $\Gamma_{mech} < 10^{-18}$ erg cm^{-3} s^{-1}, the fitting parameters for $\log_{10} G_0 = 2$ are used.

$\log_{10}[\Gamma_{mech}/\text{erg cm}^{-3}\text{ s}^{-1}]$	-24	-22	-20	-18	-16
$\log_{10}[n_c/\text{cm}^{-3}]$	0.6	1.9	3.2	4.5	5.9

Notes. For higher mechanical heating rates, those for $\log_{10} G_0 = 5$ are used since in that region of the parameter space Γ_{mech} is more relevant to high G_0.

Table 2 mark the lines in the $G_0 - n$ plane where mechanical heating is the same as the total surface heating. To the left of these lines, $\Gamma_{mech} > \Gamma_{surface}$.

In Fig. 3 the equilibrium temperature of the surface slab is shown for the range of Γ_{mech} that we consider. Regions, that are first affected by the mechanical heating input, are the ones where Γ_{mech} is comparable to the surface heating without mechanical input (see Fig. 2). This behavior can be traced by following the location of the dashed vertical lines (where $\Gamma_{mech} = \Gamma_{total,surface}$) and comparing the values of Γ_{mech} to the total surface heating contours in Fig. 3. It is clear that whenever the value of Γ_{mech} is comparable to the total surface heating, the temperature contours become almost vertical in the $n - G_0$ plane in Fig. 3. The locations where $\Gamma_{mech} = \Gamma_{total,surface}$ are marked by the dashed vertical lines where $n = n_c$ (see Table 2). For instance, in the first panel in Fig. 3 ($\Gamma_{mech} = 10^{-24}$ erg cm^{-3} s^{-1}), regions where temperatures increase significantly are when $\Gamma_{total,surface} < 10^{-24}$ erg cm^{-3} s^{-1} (see Fig. 3, and compare first panel in Fig. 3 to the middle panel in Fig. 1). Also we notice that the temperature increases from ~3000 K (for $G_0 \sim 10^2$) to ~10 000 K at the density $n = n_c$, whereas it increases from ~5000 K (for $G_0 \sim 10^{5.0}$) to ~7000 K at the same density. This can be explained by the fact that heating at the surface is mainly due to photo-electric heating, thus as G_0 increases (for a fixed n), the amount total heating increases. Hence a fixed amount of mechanical heating would contribute less to the total heating budget, leading to a lower increase in the surface temperature. Subsequent panels in Fig. 3 which correspond to higher amounts of Γ_{mech} can be interpreted in the same fashion. The main feature of these panels is the shift in the position of the line marking $n = n_c$ towards higher densities. In the last panel where $\Gamma_{mech} = 10^{-16}$ erg cm^{-3} s^{-1}, the whole parameter space is dominated by mechanical heating.

Regions with a SFR of ~1 $M_\odot$ yr^{-1} are dominated by mechanical heating up to densities of ~10^3 cm^{-3}. In Extreme starburst, where SFR of ~1000 $M_\odot$ yr^{-1} are possible, all clouds with $n < 10^{5.5}$ cm^{-3} become dominated by mechanical heating. In both cases, surface temperatures of $\gtrsim$5000 K are reached, and the temperature contours become independent of FUV heating.

3.1.2. Temperatures deep into the cloud

Now we turn our attention to the molecular region. The solution was terminated well beyond $A_V \sim 1$ mag (where mainly atomic and radicals exist) at $A_V = 20$ mag (where everything is molecular). As the FUV radiation penetrates the cloud, it is attenuated by dust absorption. Thus, the photo-electric heating that was the dominant at the surface, rapidly becomes less important and almost vanishes because (a) Γ_{photo} has a $\exp(-A_V)$ dependence on A_V; and (b) the heating efficiency ϵ becomes very small as electron abundances decrease significantly by
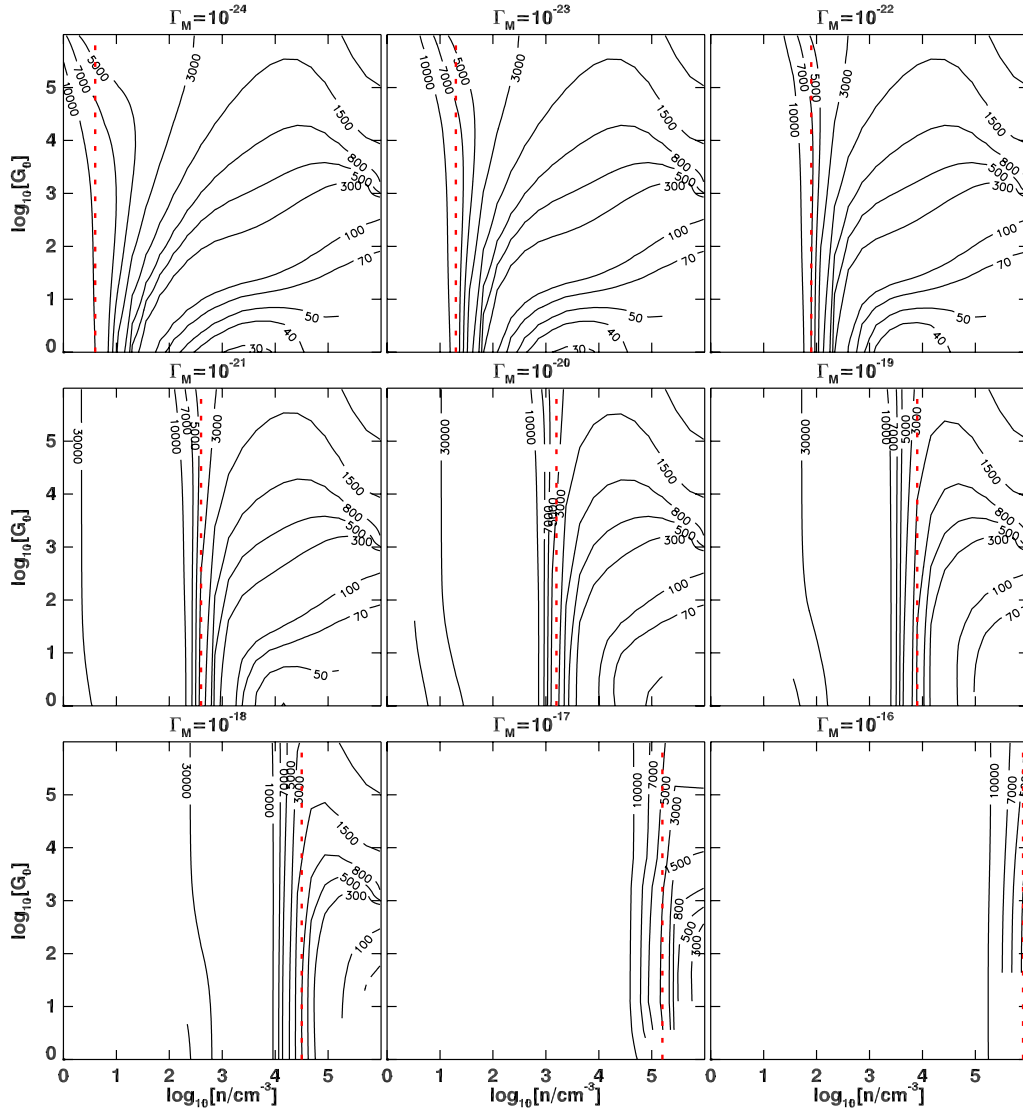
Fig. 3. Surface temperature (for $Z = Z_\odot$) for different values of mechanical heating. Each panel shows the surface temperature contours for a different value of Γ_{mech} mentioned at the top of each panel. In probing the effect of mechanical heating, each panel should be compared to the middle panel of Fig. 1 which is also for $Z = Z_\odot$. Different parts of the parameter space in n and G_0 are affected differently, depending mainly on the gas density. For $\Gamma_{mech} < 10^{-21}$ erg cm^{-3} s^{-1}, regions in density with $n < 10^3$ cm^{-3} have their temperatures increase significantly. The vertical dashed red lines mark densities $n = n_c$ where $\Gamma_{mech} = \Gamma_{total,surface}$. The location of these lines moves from very low densities ($n \sim 10^0.5$ cm^{-3}) to very high densities ($n > 10^5$ cm^{-3}) as Γ_{mech} increases from 10^{-24} to 10^{-16} erg cm^{-3} s^{-1}, sweeping the parameter space in density (for a certain grid) from left to right. In general the contour lines at $n = n_c$ become vertical, indicating that the surface temperature becomes independent of G_0. In subsequent plot, those lines are plotted only for $Z = Z_\odot$ grids, since the fits from which $n = n_c$ were derived were done only for solar metallicity.

recombination. Thus, in the absence of Γ_{mech}, heating by cosmic rays and dust (especially at high G_0) become the dominant ones in the molecular region.

In Fig. 4 we show contours of the equilibrium temperature at $A_V = 20$. In the absence of any mechanical heating, and in contrast to the situation for the surface slab, the topology of the contours is quite simple. The highest temperatures, with a maximum of ~80 K, are in the upper right corner at $n = 10^6$ cm^{-3} and $G_0 = 10^6$. Temperatures decrease monotonously along the diagonal until they reach 10 K, which is the minimum temperature we allowed for. The main characteristic of a PDR is that the surface is heated to high temperatures, which is a thin layer. Beyond this layer, in the transition zone, the temperature drops sharply. Although the temperature profile in Fig. 4 is simple, it is counter-intuitive. We might expect the temperature to decrease as the density increases at a fixed G_0, but the opposite occurs. We

explain this by the fact that as n increases, the coupling between gas and dust also increases. Dust temperature depends on G_0 and decreases as a function of A_V. Nevertheless, for very high $G_0 > 10^3$, the decreasing dust temperatures are still high enough to heat the gas (~30 K).

The temperature profile throughout the cloud is shown in Fig. 5 for the selected models M1 to M4. The temperature generally decreases as a function of A_V. For some models which have high mechanical heating rates, the temperature increases and then saturates at higher values than those obtained at for the surface. As for the models whose temperature decreases, we see that as the density decreases, more specifically as the ratio G_0/n increases, the point of saturation of the temperature gets shifted further away from the surface of the cloud ($A_V = 0$ mag). For instance, when looking at clouds illuminated with a high FUV flux of $G_0 = 10^3$, the saturation point gets shifted from
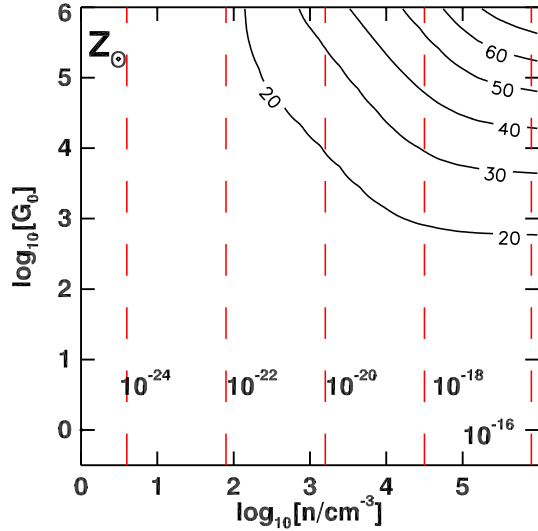
Fig. 4. Temperature at $A_V = 20$ without mechanical heating. Higher equilibrium temperatures are attained for dense molecular clouds (top right corner) with decreasing equilibrium temperature towards low n and G_0. Below the 20 K contour, all temperatures are set to 10 K – the minimum allowed in the code. The red dashed lines mark the densities $n = n_c$ where $\Gamma_{mech} = \Gamma_{total,surface}$ from Table 2.

Fig. 5. Gas temperature as a function of the visual extinction for selected models. In *the top two panels*, for $\Gamma_{mech} > 10^{-22}$ erg cm^{-3} s^{-1} (green and orange curves) the transition from H to H$_2$ does not occur. For the high density models the transition fails only for M4 when $\Gamma_{mech} > 10^{-17}$ erg cm^{-3} s^{-1}.

$A_V \sim 5$ mag for $n = 10^3$ cm^{-3} (low density gas) to $A_V \sim 2$ mag for $n = 10^{5.5}$ cm^{-3} (high density gas, compare left panels of Fig. 5). A similar behavior is seen for the right panels which have a higher FUV flux with $G_0 = 10^5$. However, we note that the saturation point remains almost constant for a fixed G_0/n, which can be seen in comparing M1 and M4, where G_0/n are on the same order of magnitude. The temperature saturation point is also related to the H/H$_2$ and C$^+$/C/CO transition zones. For example, along the lines (in $n - G_0$ parameter space) where $G_0/n = 0.003$, 1 and 300, the location of the transition zones in the chemical species are almost unchanged.

In a PDR, the total heating at the surface it is dominated by $\Gamma_{photo,A_V=0} \sim \Gamma_{total,A_V=0} = \Gamma_{surface}$, and decreases as a function of increasing A_V. Also total heating generally decreases as a function of A_V. In Sect. 3.1.1 it was demonstrated that mechanical heating increases the surface temperatures significantly whenever $\Gamma_{mech} = \Gamma_{surface}$. In such situations, since mechanical heating is added uniformly throughout the PDR, we expect it to have a stronger impact (on the physical and chemical properties) at high depths compared to those at the surface. Hence Γ_{mech} should be the most dominant heating term beyond the surface, even more dominant than heating due to cosmic rays which attains a maximum of $10^{-21.5}$ erg cm^{-3} s^{-1} for $n = 10^6$ cm^{-3}. In Fig. A.1 we show the corresponding parameter grids as a function of Γ_{mech}; the thermal profile in these grids has almost no dependence on G_0 and depends solely on n.

In order to illustrate the degree by which Γ_{mech} increases temperatures throughout the cloud, we look at the curves in Fig. 5 corresponding to $\Gamma_{mech} \neq 0$. We note that for densities where $\Gamma_{mech} = \Gamma_{surface}$, listed in Table 2, gas temperatures increase by almost two orders of magnitude for the low density models M1 and M2, and by at least one order of magnitude for the high density models M3 and M4. In fact, it suffices to have a mechanical heating rate 10 to 100 times smaller than the total heating at the cloud surface for gas temperatures to increase by a factor of ~2 (for high densities) and up to a factor of ~10 (for low densities). Thus even relatively small mechanical
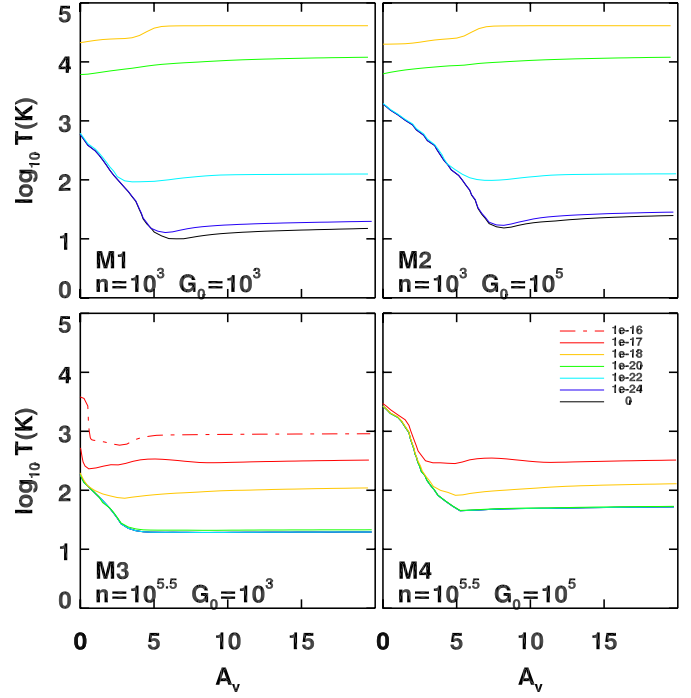
heating rates will substantially modify the physical parameters deduced from a pure PDR model. In a continuous starburst with an $SFR = 1$ $M_\odot$ yr^{-1} (which corresponds to $\Gamma_{mech} \sim 2 \times 10^{-20}$ erg cm^{-3} s^{-1} using Eq. (1)), the mechanical luminosity (heating) is about 1% of the bolometric luminosity (Leitherer et al. 1999). Which implies that the ratio of mechanical luminosity to UV luminosity (where the emission of star forming regions peak) is larger than 1%. Especially if we consider higher a $SFR \sim 10$ $M_\odot$ yr^{-1} which translates to a $\Gamma_{mech} \sim 2 \times 10^{-19}$ erg cm^{-3} s^{-1}. Assuming that half the UV radiation is absorbed by the ISM of the galaxy, we would still be in the range where Γ_{mech} is at least 1% of the surface heating (which is due to UV radiation), thus significantly altering the equilibrium temperatures of PDRs.

3.2. Molecular gas tracers

Now that we have determined the degree to which mechanical heating alters the thermal properties of PDRs, we examine its effect on the chemical properties. Molecular clouds consist mainly of molecular hydrogen which is not directly observable except under very special circumstances. Thus, we must depend on the (sub)millimeter line emission from various transitions of much less abundant tracer molecules. Each molecular line represents its own critical density and temperature.

In the following sections, we will consider the effect of mechanical heating on a few species commonly used as tracers. These are CO for relatively low gas densities and HCO$^+$, HCN, and HNC for relatively high densities, in addition to H$_2$O which has been also recently observed in very dense gas environments $n \sim 10^6$ cm^{-3}.
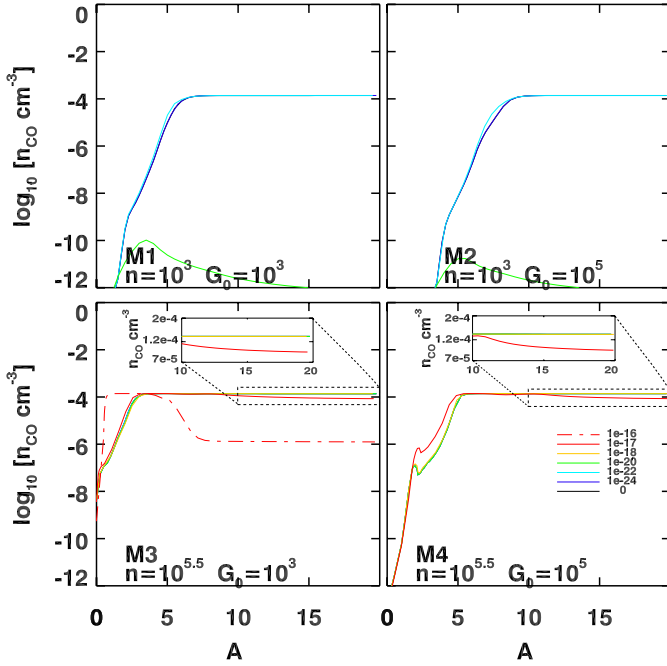
Fig. 6. CO abundance as a function of A_V for selected models. In all the diagrams, the C/CO transition zone is shifted towards the surface as a function of increasing Γ_{mech}. For M1 and M2, the abundance of CO is below the displayed range for $\Gamma_{mech} > 10^{-20}$ erg cm^{-3} s^{-1} (these curves are not shown). The other curves almost overlap except for $\Gamma_{mech} = 10^{-20}$ erg cm^{-3} s^{-1}. In models M3 and M4 the abundance of CO drops slightly beyond the transition zone compared to the case of no mechanical heating. The curves overlap except for $\Gamma_{mech} = 10^{-16}$ erg cm^{-3} s^{-1} where the C$^+$/C/CO transition does not fully take place.

3.2.1. CO

Properties of molecular H$_2$ gas are generally studied through observations of CO, which is the next most abundant species. The critical density (n_{cr}[5]) for the ground-state $J = 1-0$ ^{12}CO transition is $n_{cr} \sim 2000$ cm^{-3}. This is in the middle section of range of densities n considered in our grids. Thus, the response of CO to mechanical heating may have important consequences for estimates of the amount of molecular gas and, for instance, may also explain the high gas temperature of $100-150$ K which have been estimated for molecular gas in the centers of galaxies with densities of $100-1000$ cm^{-3} (Israel 2009).

In Fig. 6 we show the abundance of CO as a function of depth inside the cloud. For the models with densities close to n_{cr} (M1 and M2), CO abundances decrease sharply for $\Gamma_{mech} > 10^{-18}$ erg cm^{-3} s^{-1} and almost disappears when $\Gamma_{mech} > 10^{-20}$ erg cm^{-3} s^{-1}, where $x_{CO} < 10^{-13}$ caused by very high temperatures $T > 10\,000$ K (abundances of species relative to the total number of hydrogen nuclei are denoted by $x_i = n_i/(n_H + 2n_{H_2})$). At such high temperatures, no molecules, including CO, are formed. This is due to the very low abundance of H$_2$ which drops from $\sim$0.5 to $\sim 10^{-9}$ beyond the radical region. This drop breaks the chemical network which leads to the formation of CO. In addition, the higher abundances of the ionic species H$_3^+$ and He$^+$ enhance the destruction of CO through the reactions H$_3^+$ + CO $\rightarrow$ HCO$^+$ + H$_2$ and He$^+$ + CO $\rightarrow$ O + C$^+$ + He. On the other hand, for $\Gamma_{mech} \leq 10^{-18}$ erg cm^{-3} s^{-1} the first obvious effect of mechanical heating on CO is the shift of the C/CO transition

---

[5] The critical density n_{cr} should not be confused with n_c, defined earlier, which is the gas density where $\Gamma_{mech} = \Gamma_{total,surface}$.
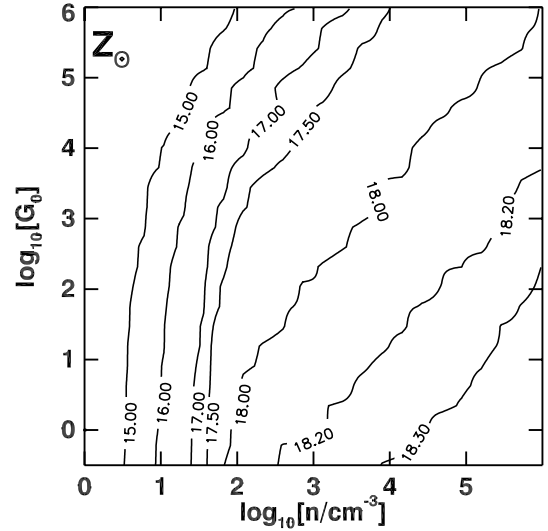
Fig. 7. CO total column density up to N(H) $= 1.8 \times 10^{22}$ cm^{-2} or $A_V \sim 10$ mag for $Z = Z_\odot$ without mechanical heating.

zone towards the surface of the slab. This shift is caused by the enhanced abundance of O$_2$ and OH and higher temperatures in the radical region (see Fig. 6).

In the high density models M3 and M4, the abundance of CO decreases by a factor of two as Γ_{mech} increases from 10^{-18} erg cm^{-3} s^{-1} to 10^{-17} erg cm^{-3} s^{-1}. As Γ_{mech} is pushed further to 10^{-16} erg cm^{-3} s^{-1} x_{CO} decreases from 10^{-4} to 10^{-16} for M3 and becomes under-abundant for M4 ($x_{CO} < 10^{-12}$). This behavior can be explained by the enhanced abundance of the ionized species He$^+$ and H$_3^+$, which destroy CO through ion-neutral reactions. Also, the significant drop in abundance of H and HCO (by three orders of magnitude) reduce the formation of CO through the reactions H + HCO $\rightarrow$ CO + H$_2$ and O + C$_2$ $\rightarrow$ CO + C.

In Figs. 7 and A.2, the column density of CO is shown without and with increasing values of mechanical heating respectively. The general trend is an increase in N(CO) whenever the added Γ_{mech} is comparable to the surface heating of a PDR with no mechanical heating. This occurs at densities (n_c) marked by vertical dashed lines in Fig. A.2. For higher densities in the grids (to the right of these lines) $\Gamma_{mech} < \Gamma_{surface}$ and the opposite is true for lower densities (to the left the lines). At densities a factor of 3 higher than n_c (a distance of 0.5, in $\log_{10}$ scale, to the right of n_c) where $\log_{10} n = \log_{10} n_c + 0.5$ we can see a change in the shape of the contours in N(CO). This change corresponds to an increase up to a factor of two in N(CO), with no noticable change in regions where $\log_{10} n > \log_{10} n_c + 0.5$. From our fits of surface heating these regions have $\Gamma_{surface} < \Gamma_{mech}/20$. It is also noticed that the increase of N(CO) is more pronounced for high values of G_0/n as Γ_{mech} increases (compare left and right panel of Fig. 6). We can explain this by looking at the C$^+$/C/CO transition zone, which gets shifted towards the surface of the cloud as Γ_{mech} dominates. This shift is more pronounced for higher G_0, thus resulting in more CO in the column of H we are considering (N(H) $= 1.8 \times 10^{22}$ cm^{-2}).

For conditions similar to that of the Milky Way, $SFR \sim 1$ $M_\odot$ yr^{-1} which corresponds to a Γ_{mech} of 2×10^{-20} erg cm^{-3} s^{-1}, N(CO) estimates would be marginally ($\sim$20%) lower when Γ_{mech} is not taken into account. However, for starbursts with $n \sim 10^4$ cm^{-3} and $G_0 \sim 10^3$ and a significantly higher SFR ($\sim$50 $M_\odot$ yr^{-1}) the N(CO) estimates would be a factor of two less when the Γ_{mech} of 1×10^{-18} erg cm^{-3} s^{-1} is

ignored (compare Fig. 7 to the panel corresponding to $\Gamma_{mech} = 10^{-18}$ erg cm^{-3} s^{-1} in Fig. A.2, where the N(CO) contour is shifted to the right, from $n \sim 10^3$ to $n \sim 10^{4.5}$ cm^{-3}). For low metallicity grids we considered $Z = 0.5 \, Z_\odot$, which may represent systems such as dwarf galaxies (where the metallicity may be as low as $0.1 \, Z_\odot$), the increase in N(CO) may be up to one order of magnitude, reaching 10^{17} cm^{-2}. This occurs even for a low mechanical heating rates corresponding to an SFR of $\sim 1 \, M_\odot$ yr^{-1}. The increase in N(CO) is visible in the central part of the parameter space (compare the grids when $\Gamma_{mech} = 10^{-21}$ erg cm^{-3} s^{-1} and $\Gamma_{mech} = 10^{-20}$ erg cm^{-3} s^{-1} in Fig. A.4). In contrast, for the highest metallicity we considered, the $Z = 2 \, Z_\odot$ grids, which represents a more likely condition for galactic centers, the increase is less prominent even for the extreme mechanical heating rates of $\Gamma_{mech} = 10^{-17}$ erg cm^{-3} s^{-1} corresponding to $\sim 500 \, M_\odot$ yr^{-1} (see Fig. A.3).

Thus, we conclude that we would potentially severely underestimate the amount of CO in the system if mechanical heating is ignored, especially for metallicities less than $Z_\odot$, i.e. in dwarf galaxies.

3.2.2. H$_2$O

Until the launch of the *Herschel* Space Observatory, it was not possible to observe water lines in the far-infrared from extragalactic sources, as their emission is blocked by the Earth's atmosphere. Now, water line emission has been detected by several *Herschel* key programs, and a striking example is provided by the water lines observed in Markarian 231 (González-Alfonso et al. 2010). In this object, water lines intensities are comparable to those of the CO lines. This is very different from what is observed for, e.g., the star-burst galaxy M82 (Weiß et al. 2010) and the Orion Bar in the Milky Way (Habart et al. 2010).

Water can be formed through a neutral-neutral reaction chain, $O + H_2 \rightarrow OH + H$, followed by $OH + H_2 \rightarrow H_2O + H$. In order to obtain significant abundances, the medium has to be molecular and sufficiently warm, as the reactions have barriers of ~ 2000 K. In X-ray exposed environments, it is possible to obtain a significant water abundance $x_{H_2O} \sim 10^{-10}$ at high temperatures ($T \sim 3000$ K), produced by an ion-molecule reaction chain. A recent paper by Meijerink et al. (2011) shows that water production can be enhanced by an order of magnitude in these warm atomic environments, when the grains are stripped from their ice layers, as is possibly the case in violent environments around an AGN.

As we have seen in the previous sections, the temperatures in the molecular regions of the mechanically heated PDR can be increased to temperatures $T \gg 100$ K, which is favorable for the production of water through the neutral reaction chain.

In Fig. 8 the abundance of H$_2$O is shown as a function of depth. The low-density models are marginally affected as long as $\Gamma_{mech} < 10^{-20}$ erg cm^{-3} s^{-1}. For higher mechanical heating rates the H/H$_2$ transition does not occur, thus H$_2$O does not form. However, the impact on the abundance of H$_2$O is more significant for the high-density (M3 and M4), where the abundance of H$_2$O is enhanced by at least one order of magnitude when $\Gamma_{mech} > 10^{-17}$ erg cm^{-3} s^{-1}. The reference grid for the column density of H$_2$O at solar metallicity (without mechanical) heating is shown in Fig. 9. In comparing this reference grid to Figs. A.5–A.7 (corresponding to grids for lower and higher metallicities), the column densities range between N(H$_2$O) $\sim 10^{14}$ (very low densities, $n < 10^1$ cm^{-3}) and up to $10^{16.5}$ cm^{-2} ($n > 10^2$ cm^{-3}). These column densities increase when the gas density if close to $n = n_c$ especially for
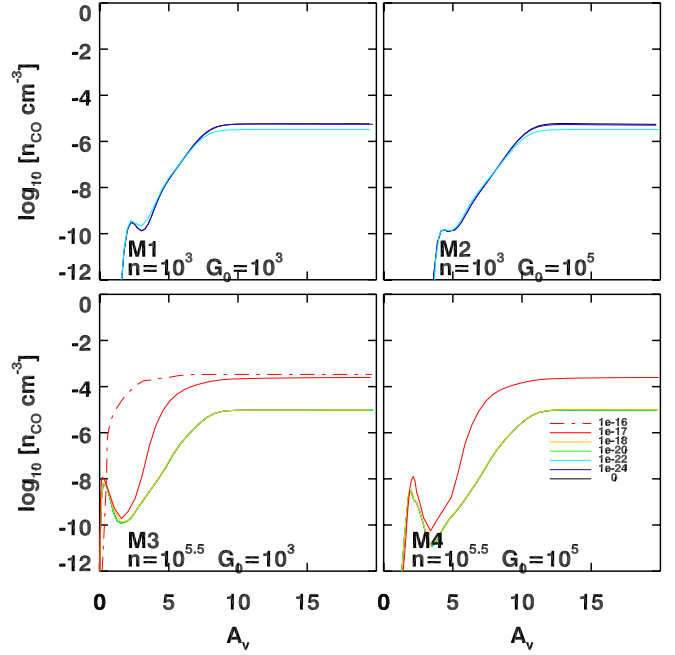

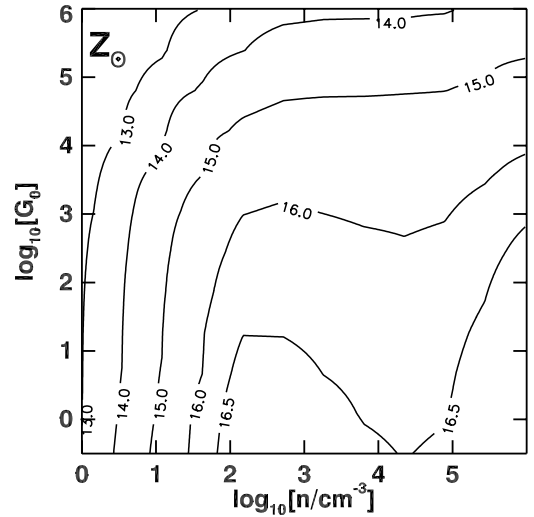**Fig. 8.** H$_2$O abundance as a function of A_V for selected models.

Fig. 9. H$_2$O total column density up to N(H) $= 1.8 \times 10^{22}$ cm^{-2} or $A_V \sim 10$ mag for $Z = Z_\odot$ without mechanical heating.

$\Gamma_{mech} > 10^{-19}$ erg cm^{-3} s^{-1} where an optimum of (N(H$_2$O) $\sim 10^{18}$ cm^{-2}) is reached (see last row of Fig. A.5). When the mechanical heating rate becomes too high (in the regions where $n \ll n_c$), the column densities drop again, because there is insufficient H$_2$, which is destroyed through collisional dissociation, to form water. Therefore, one finds that this optimum moves from lower to higher densities for increasing mechanical heating rates.

Thus, the high column densities of H$_2$O accompanied by high temperatures make this molecule an excellent diagnostic tool for galaxy environments where mechanical heating dominates.

3.2.3. HCN and HNC

The critical density for the HCN and HNC $J = 1-0$ collisional excitation by H is $\sim 1 \times 10^6$ and $\sim 0.5 \times 10^6$ cm^{-3} respectively.

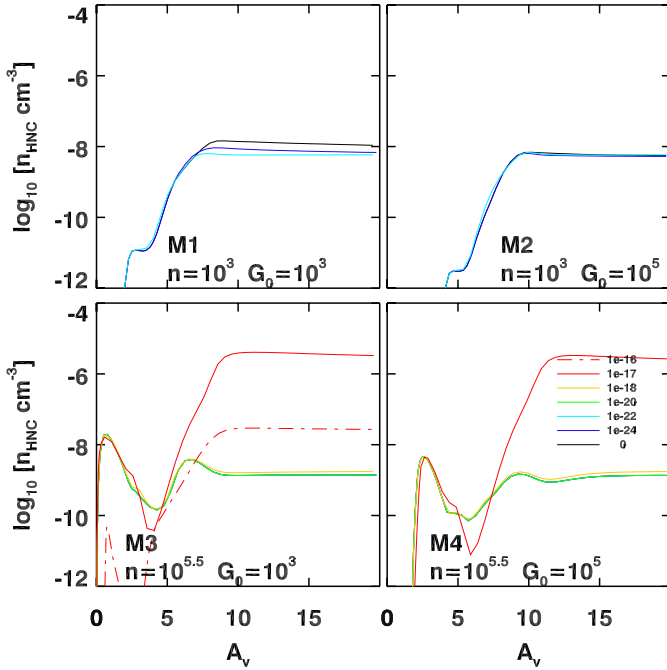**Fig. 10.** HNC abundance as a function of A_V for selected models. In *the top panels* the curves for $\Gamma_{mech} > 10^{-22}$ erg cm^{-3} s^{-1} are not shown since the C$^+$/C/CO transition does not take place.
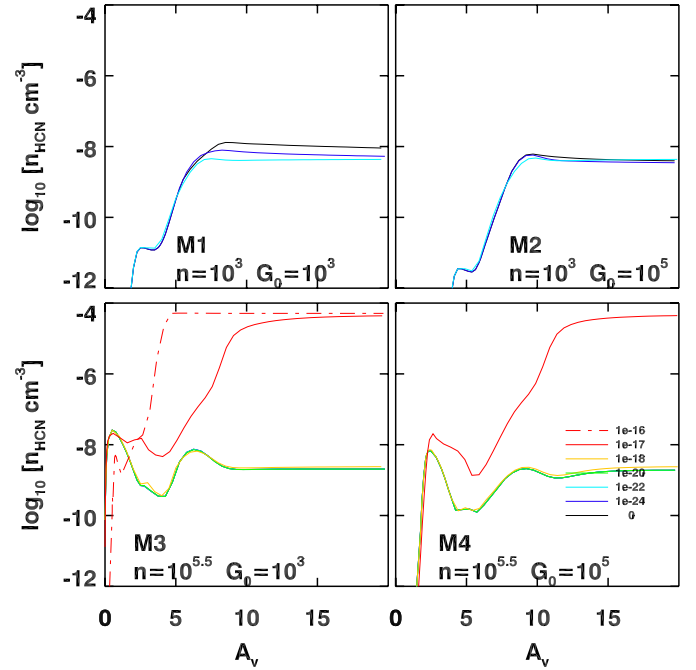

Fig. 11. HCN abundance as a function of A_V for selected models. The same convention of Fig. 10 are used.

Together with their relatively high abundance, makes them valuable high gas density tracers. Here we will be first looking at the abundances of HNC and HCN, x_{HNC} and x_{HCN} respectively up to $A_V = 20$ mag. Then we will study the effect of mechanical heating on the column density ratios of these two species.

Although included for completeness in Figs. 10 and 11, the low-density models M1 and M2 are of no physical interest, since they refer to densities at least two order of magnitude below the critical density of HCN and HNC. The more relevant high-density models M3 and M4 show (in contrast to the low-density models), an increase by four orders of magnitude in x_{HCN} when Γ_{mech} exceeds 10^{-18} erg cm^{-3} s^{-1}; whereas an increase of three orders in x_{HNC} is observed. The increase in the abundance of HCN was also noted by Loenen et al. (2008) and Meijerink et al. (2011). Mechanical heating causes the equilibrium temperature, in the molecular region, to increase from 100 K, when $\Gamma_{mech} = 10^{-18}$ erg cm^{-3} s^{-1}, to ~900 K when $\Gamma_{mech} = 10^{-16}$ erg cm^{-3} s^{-1} (see Fig. 5). Consequently HNC is converted more effectively to HCN via the reaction HNC + H → HCN + H whose activation barrier of ~200 K is surpassed (Schilke et al. 1992). This explains the drop in the fractional abundance of HNC with respect to HCN with $x_{HNC}/x_{HCN} \sim 0.1$.

The abundance of HCN and HNC increases by few orders of magnitude with increasing Γ_{mech}. This increase is because of the enhanced production of both species via the neutral-neutral reaction H$_2$ + CN → HCN + H. Also HCN and HNC are formed with equal probability through recombination reactions of HCNH$^+$, which has been also noted by Aalto (2005). These two processes are more dominant than the reaction HNC + H → HCN + H, which is just a re-shuffling the bonds of HNC that leaves x_{HCN} + x_{HNC} constant. However HNC + H → HCN + H is responsible for the bias in the abundance of HCN with respect to HNC.

Now we look at the column density ratio $N(HNC)/N(HCN)$ in order to gauge the effects of mechanical heating in the $G_0 - n$ parameter space. These are computed by integrating x_{HNC} and x_{HCN} up to $N(H) = 1.8 \times 10^{22}$ cm^{-2} and taking their ratio.
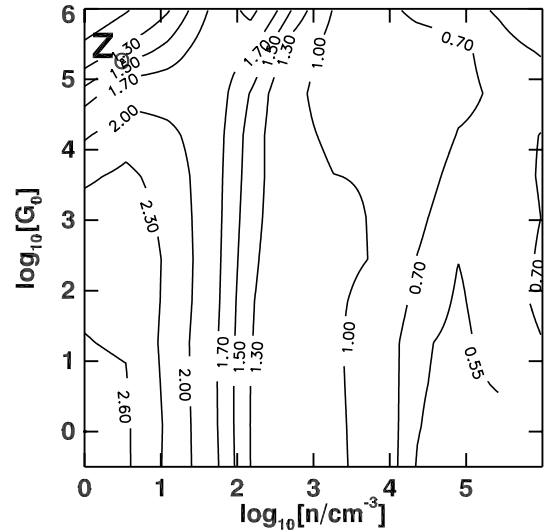

Fig. 12. HNC/HCN integrated column density ratios (integrated up to $N(H) = 1.8 \times 10^{22}$ cm^{-2} or $A_V \sim 10$ mag for $Z = Z_\odot$) without mechanical heating. The column density ratio decreases from left to right. For dense molecular clouds, the ratio is ~0.7 and it is almost constant as a function of G_0.

The same column density is considered for the other metallicities when the ratio $N(HNC)/N(HCN)$ is computed. In Fig. 12 the column density ratio of HNC to HCN is shown for the whole grid with no mechanical heating (pure PDR). Since HCN is a good tracer for dense molecular clouds with $n \geq 10^4$ cm^{-3} (Solomon et al. 1992), we focus on that part of the parameter space for this diagnostic. In the absence of mechanical heating, in this range of density, $N(HNC)/N(HCN) < 1$ for all G_0. When mechanical heating is added, specifically for Γ_{mech} larger than 10^{-19} erg cm^{-3} s^{-1}, the column density ratio starts decreasing even more with almost no dependence on G_0. For instance, in the upper right corner $N(HNC)/N(HCN)$ decreases from 0.7 to 0.55 (see Fig. A.8). This decrease affects regions

where $\log_{10} n = \log_{10} n_c + 1.0$. At $\log_{10} n = \log_{10} n_c$ (dashed vertical lines in Fig. A.8) $\Gamma_{mech} = \Gamma_{surface}$ as described in Sect. 3.1.1, so mechanical heating dominates everywhere in the cloud. Whereas at $\log_{10} n = \log_{10} n_c + 1.0$ mechanical heating is up to 100 times smaller than the total heating at the surface of the pure PDR case. For the largest Γ_{mech} considered 10^{-16} erg cm^{-3} s^{-1} the $N(HNC)/N(HCN)$ decreases below 0.1 over the whole parameter space (see Fig. A.8). This is also observed for the other metallicities in Figs. A.10 and A.9.

Thus, we find that the ratio $N(HNC)/N(HCN)$ is sensitive to low mechanical heating rates, a factor of a hundred smaller than the total heating at the surface of a pure PDR. For higher mechanical heating rates that are 20 times smaller than those at the surface, $N(HNC)/N(HCN)$ decrease at least by a factor of two.

3.2.4. HCN/HCO$^+$

HCO$^+$ is another high density gas tracer with $n_{cr} \sim 10^5$ cm^{-3} for $J = 1{-}0$ transition. It has been suggested that in AGNs, where X-ray heating dominates, HCN is less abundant than HCO$^+$ (Lepp & Dalgarno 1996), suggesting that the HCN/HCO$^+$ ratio is a diagnostic for the determination of the physical nature of a source object. A detailed study of the effect of cosmic rays (Meijerink et al. 2011) shows that the abundance of HCO$^+$ is inhibited by high cosmic ray rates. Since cosmic rays have a large penetrating depth, they may raise the temperature of clouds up to large column densities. Since Γ_{mech} is added uniformly throughout the slab and the temperatures are likewise enhanced, a behavior similar to that caused by cosmic rays should be seen. In a similar fashion as for HNC and HCN, we look at abundances and column density ratios with and without mechanical heating to see how it affects the $N(HCN)/N(HCO^+)$ ratios.

In the low- density models (top row of Fig. 13) a slight increase in the abundance of HCO$^+$ is observed up to $\Gamma_{mech} = 10^{-22}$ erg cm^{-3} s^{-1}. This is caused by a slightly slower destruction rate of HCO$^+$ through the reaction $HCO^+ + e^- \rightarrow CO + H$. For $\Gamma_{mech} > 10^{-22}$ erg cm^{-3} s^{-1}, the two orders of magnitude drop in the abundance of HCO$^+$ in the molecular region is caused mainly by ion-neutral reactions with H$_2$O, HCN (which we demonstrated to increase in the previous section) and C. The abundance of HCO$^+$ is unaffected by Γ_{mech} in M3 and M4 unless it is larger than 10^{-17} erg cm^{-3} s^{-1}. For that amount of mechanical heating x_{HCO^+} becomes $\sim 10^{-11}$ beyond the radical region. In this case, the reactions $H_2O + HCO^+ \rightarrow CO + H_3O^+$ and $HCN + HCO^+ \rightarrow HCNH^+ + CO$ dominate (again because of enhanced abundances of H$_2$O and HCN) in destroying HCO$^+$ by two orders of magnitude compared to the other reactions. However an increase of one to four orders of magnitude in x_{HCO^+} is observed for $A_V < 5$ mag. This contributes significantly to the column density of HCO$^+$ in clouds with low $N(H)$, which could make a significant impact on the interpretation of line ratios for clouds with small column densities as opposed to those with high $N(H)$.

Looking at the column density ratios of HCN to HCO$^+$, $N(HCN)/N(HCO^+)$, we see in Fig. 14 a non-trivial dependence. The ratio varies from $10^{-0.7}$ (in the high-density and high-UV flux zone) to $10^{0.7}$ (in the high-density, moderate- to low-UV flux zone).

An interesting feature of this column density ratio, quite different from the HNC/HCN situation, is the fact that the $N(HCN)/N(HCO^+)$ ratio increases to ~ 10 and $\sim 10^3$, as opposed to a decrease of *only* a factor of two in the ratio $N(HNC)/N(HCN)$ as a function of increasing Γ_{mech}. For high densities when $\Gamma_{mech} > 10^{-20}$ erg cm^{-3} s^{-1} the contours
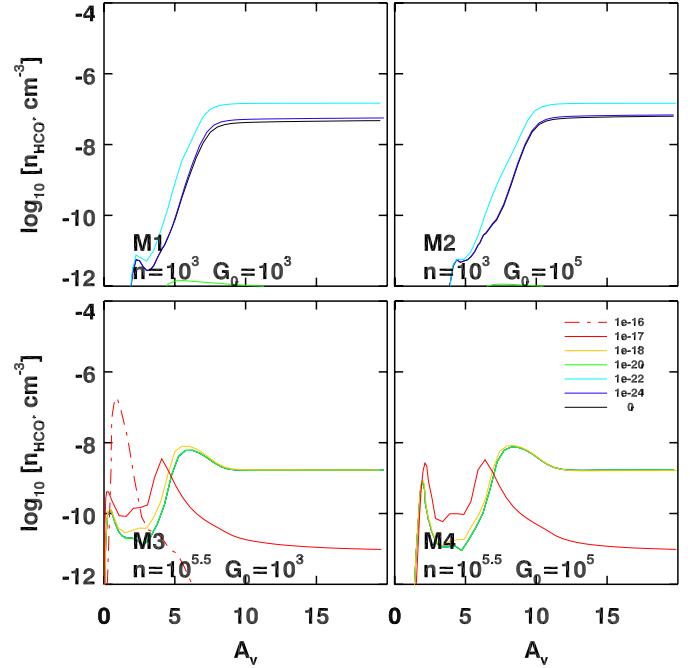

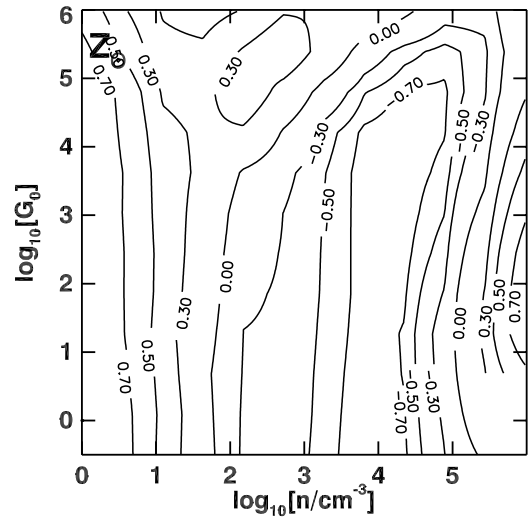**Fig. 13.** HCO$^+$ abundance as a function of A_V for selected models.

Fig. 14. HCN/HCO$^+$ integrated column density ratios (integrated up to $N(H) = 1.8 \times 10^{22}$ cm^{-2} or $A_V \sim 10$ mag for $Z = Z_\odot$) without mechanical heating.

become almost parallel for $\log_{10} n_c < \log_{10} n < \log_{10} n_c + 1.0$. This implies that the $N(HCN)/N(HCO^+)$ ratio does not depend on G_0/n (as far as this ratio is concerned), but is dominated by mechanical heating down to values ~ 100 times smaller than the surface heating of a pure PDR. This is shown in Fig. A.11 where $N(HCN)/N(HCO^+)$ ranges between 10 and 10^4 in the density range mentioned. Similar behavior is seen for the other metallicities considered.

This, and the fact that $N(HCN)/N(HCO^+)$ is very sensitive to very small values of mechanical heating makes this ratio an excellent diagnostic for mechanically heated regions.

4. Conclusion and discussion

The goal of this paper is to assess when we should take into account mechanical heating in modeling the observed line

emission properties of the interstellar medium in PDRs. We have calculated the equilibrium thermal and chemical properties of interstellar clouds as 1D semi-infinite slabs for a large range of hydrogen gas densities ($1 < n < 10^6$ cm^{-3}) and radiation fields ($0.3 < G_0 < 10^6$). As a result, we covered more or less *all* conditions physically relevant for the ISM, from the diffuse ISM in the outskirts of quiescent galaxies ($G_0 < 1$, $n = 1$–100 cm^{-3}), to the dense, UV-exposed environments ($G_0 \sim 10^5$, $n \sim 10^{5.5}$ cm^{-3}) of active galaxy centers. We have also explored three levels of heavy-element abundance, $Z = 0.5$, 1.0 and 2.0 $Z_\odot$, thus considering the low metallicities of dwarf galaxies as well as the enhanced metallicities in galaxy centers. We have done this by adding a mechanical heating term resulting from dissipating turbulence of supernovae. The heating rates included are between $10^{-24} < \Gamma_{\text{mech}} < 10^{-16}$ erg cm^{-3} s^{-1}, which corresponds to star-formation rates ranging from $SFR \sim 0$ to ~ 1000 $M_\odot$ yr^{-1} under the assumptions explained in Sect. 2.1. We first explored the effect on the thermal balance at the surface and deep into the cloud at high column densities, and then the chemistry of a few commonly observed species in the ISM of galaxies, namely, CO, H$_2$O, HCN, HNC, and HCO$^+$. We demonstrated that mechanical heating radically changes the resulting chemical and thermal structure. The following conclusions can be drawn:

(i) The equilibrium temperature in a PDR is significantly altered, i.e., increased by an order of magnitude, for ratios $\Gamma_{\text{mech}}/n^{1.5} \sim 10^{-25}$ erg cm$^{-4.5}$ s^{-1}. This is a lower bound in the sense that when $\Gamma_{\text{mech}}/n^{1.5} = 10^{-25}$ the temperature inside the cloud (even for the densest clouds $n \sim 10^6$ cm^{-3}) increases by a factor of 10. Thus, Γ_{mech} *must* be taken into account while solving for the equilibrium state of a PDR. In translating this relation into one relating gas density to the star formation rate, it can be expressed as $SFR/n^{3/2} = 7 \times 10^{-6}$. For higher values the temperature increases even more. Also, the H/H$_2$ transition may not occur for very high mechanical heating rates ($\Gamma_{\text{mech}}/n^{1.5} \gg 10^{-25}$), especially for the low density clouds with $n \sim 10^3$ cm^{-3}.

(ii) Mechanical heating rates that are two orders of magnitudes smaller than the surface heating nevertheless are high enough to increase the temperature by an order of magnitude in low-density clouds and up to a factor of two in high-density clouds $n \sim 10^6$ cm^{-3}. For instance, inclusion of a mechanical heating rate of 10^{-18} erg cm^{-3} s^{-1} in the high-density cloud models M3 and M4 of Meijerink & Spaans (2005) increases the temperatures inside the clouds from $T \sim 30$ K to ~ 100 K and from $T \sim 70$ K to ~ 110 K, respectively. Such heating rates Γ_{mech} are expected to occur in star-burst galaxies, and correspond to an SN rate of approximately 0.3 per year and an SFR rate of 9.4 $M_\odot$ yr^{-1} (Loenen et al. 2008).

(iii) We observe that N(CO) is easily doubled when mechanical heating is included in modeling PDRs, especially for gas with $n \sim 10^3$ cm^{-3}. As such, mechanical heating should be considered, when interpreting observed CO data. We also observe that the implied column density strongly depends on metallicity. This column density decreases from 10^{18} cm^{-2} at solar metallicity to 10^{17} cm^{-2} at half-solar metallicity; whereas it increases up to 10^{19} cm^{-2} at double-solar metallicity. This is particularly interesting for galaxy centers where the metallicity is expected to be higher than that of the solar neighborhood.

(iv) Our results show that the brightness of emission lines observed in galaxy centers may at least partly be due to high mechanical heating rates. The models with $Z = 2 Z_\odot$ require

higher column densities, and temperatures are enhanced by a factor 2 to 10. It also suggests that CO column densities in low-metallicity dwarf galaxies are even lower than assumed otherwise. Mechanical heating excites the gas to high temperatures, but the column density N(CO) is significantly lower (by almost an order of magnitude) compared to $Z = Z_\odot$. In addition to that, the relative gas fraction is lower in dwarf galaxies, as supernovae easily disperse gas from the galaxy.

(v) Like CO, H$_2$O also exhibits an increase in column density. The temperature increase induced by mechanical heating results in implied column densities N(H$_2$O) three orders of magnitude higher (up to $\sim 10^{18}$ cm^{-2}) compared to models without mechanical heating. This gives H$_2$O approximately the same column density as CO, for the highest mechanical heating rate. Based on this, H$_2$O lines could also provide an excellent diagnostic in combination with CO, when studying mechanical heating in galaxies.

(vi) HCN, HNC, HCO+ line ratios have been used to discriminate between PDRs and XDRs (Meijerink et al. 2007; Loenen et al. 2008). Although we do not compute line intensity ratios in this paper, we have studied the signature of mechanical heating on the integrated column density ratios of HNC/HCN and HCN/HCO+. We find that model HNC/HCN column density ratios decrease by a factor of at least 5 for gas densities $n > 10^5$ cm^{-3}, when $\Gamma_{\text{mech}} > 10^{-17}$ erg cm^{-3} s^{-1}. This effect is mitigated in clouds subjected to lower mechanical rates, but only at densities $n < 10^4$ cm^{-3}. HCN and HNC do not produce significant line emission at these densities as they are well below the critical density for excitation. On the other hand, the HCN/HCO$^+$ column density ratio strongly depends on mechanical heating. This ratio increases from ~ 10 to ~ 100, for dense molecular clouds ($n > 10^5$ cm^{-3}), when $\Gamma_{\text{mech}} = 10^{-19}$ erg cm^{-3} s^{-1} and up to 10^4 for $\Gamma_{\text{mech}} = 10^{-18}$ erg cm^{-3} s^{-1} for $Z = 0.5$, 1.0, 2 $Z_\odot$. In general for these conditions the column densities of HCO$^+$ decrease from $\sim 10^{14}$ cm^{-2} to $\sim 10^{13}$ cm^{-2}, those for HCN increase from $\sim 10^{13}$ cm^{-2} to $\sim 10^{16.5}$ cm^{-2}, whereas N(HNC) drop to $\sim 10^{13}$ cm^{-2} from $\sim 10^{14}$ cm^{-2}. The abundance of HCO$^+$ drops by at least three orders of magnitude at column densities higher $N_{\text{H}} > 1.8 \times 10^{21}$ cm^{-2} for the aforementioned Γ_{mech}. In galaxy centers, higher A_{V} are easily possible compared to $Z = Z_\odot$. This translates into higher N(H), which in turn would imply a smaller N(HCO$^+$) compared to N(HCN). Hence resulting in even higher HCN/HCO+ column density ratio. The lack of HCO$^+$ in combination with bright HCN line emission might be useful in tracing regions with high mechanical heating rates.

The integrated column density ratios do not translate directly into line intensity ratios. Instead, one should compute these ratios by solving the radiative transfer equations. We will consider predictions for the actual line intensities of HCN, HNC and HCO$^+$ in the next paper, where we will also assess time-dependent effects. The equilibrium treatment is certainly valid for the low-metallicity dwarf galaxies, and the benchmark-metallicity of solar neighborhood galaxy disks, but this may not be the case for the high-metallicity galaxy centers, where the chemical, thermal, and dynamical timescales are quite comparable in the inner <100 pc, especially at densities $n < 10^3$ cm^{-3}. For example, the formation timescale of H$_2$ (Hollenbach & Tielens 1999) is <5 Myr at an ambient gas density $n \sim 10^3$ cm^{-3}

and a kinetic temperature of $T \sim 100$ K. The stellar orbital periods (which stir up the ISM) are comparable to or shorter than this, namely between 0.1 and 15 Myr. Hence, a time-dependent treatment is necessary, and we aim to accomplish this in upcoming papers by adapting the current PDR-XDR code. We will allow for time-dependent chemical evolution, and couple it with an SPH code through AMUSE. As such, the chemistry, gas and stellar dynamics are being evolved self-consistently.

References

Aalto, S. 2005, in Astrochemistry: Recent Successes and Current Challenges, ed. D. C. Lis, G. A. Blake, & E. Herbst, IAU Symp., 231, 261
Bakes, E. L. O., & Tielens, A. G. G. M. 1994, ApJ, 427, 822
Bayet, E., Williams, D. A., Hartquist, T. W., & Viti, S. 2011, MNRAS, 414, 1583
Black, J. H., & Dalgarno, A. 1977, ApJS, 34, 405
Bohlin, R. C., Savage, B. D., & Drake, J. F. 1978, ApJ, 224, 132
Dahlén, T., & Fransson, C. 1999, A&A, 350, 349
de Jong, T., Boland, W., & Dalgarno, A. 1980, A&A, 91, 68
González-Alfonso, E., Fischer, J., Isaak, K., et al. 2010, A&A, 518, L43
Habart, E., Dartois, E., Abergel, A., et al. 2010, A&A, 518, L116
Habing, H. J. 1969, Bull. Astron. Inst. Netherlands, 20, 177
Hollenbach, D. J., & Tielens, A. G. G. M. 1999, Rev. Mod. Phys., 71, 173
Israel, F. P. 2009, A&A, 506, 689
Kaufman, M. J., Wolfire, M. G., Hollenbach, D. J., & Luhman, M. L. 1999, ApJ, 527, 795
Kroupa, P. 2001, MNRAS, 322, 231
Leitherer, C., Schaerer, D., Goldader, J. D., et al. 1999, ApJS, 123, 3
Lepp, S., & Dalgarno, A. 1996, A&A, 306, L21
Loenen, A. F., Spaans, M., Baan, W. A., & Meijerink, R. 2008, A&A, 488, L5
Maloney, P. R., Hollenbach, D. J., & Tielens, A. G. G. M. 1996, ApJ, 466, 561
Meijerink, R., & Spaans, M. 2005, A&A, 436, 397
Meijerink, R., Spaans, M., & Israel, F. P. 2007, A&A, 461, 793
Meijerink, R., Spaans, M., Loenen, A. F., & van der Werf, P. P. 2011, A&A, 525, A119
Papadopoulos, P. P. 2010, ApJ, 720, 226
Pelupessy, F. I. 2005, Ph.D. Thesis, Leiden Observatory, Leiden University, The Netherlands
Pelupessy, F. I., & Portegies Zwart, S. 2012, MNRAS, 420, 1503
Pérez-Beaupuits, J. P., Wada, K., & Spaans, M. 2011, ApJ, 730, 48
Portegies Zwart, S., McMillan, S., Harfst, S., et al. 2009, New A, 14, 369
Röllig, M. 2011, A&A, 530, A9
Röllig, M., Ossenkopf, V., Jeyakumar, S., Stutzki, J., & Sternberg, A. 2006, A&A, 451, 917
Schilke, P., Walmsley, C. M., Pineau Des Forets, G., et al. 1992, A&A, 256, 595
Solomon, P. M., Downes, D., & Radford, S. J. E. 1992, ApJ, 387, L55
Tielens, A. G. G. M., & Hagen, W. 1982, A&A, 114, 245
Tielens, A. G. G. M., & Hollenbach, D. 1985, ApJ, 291, 722
Wada, K., & Norman, C. A. 2002, ApJ, 566, L21
Wada, K., & Tomisaka, K. 2005, ApJ, 619, 93
Weiß, A., Requena-Torres, M. A., Güsten, R., et al. 2010, A&A, 521, L1
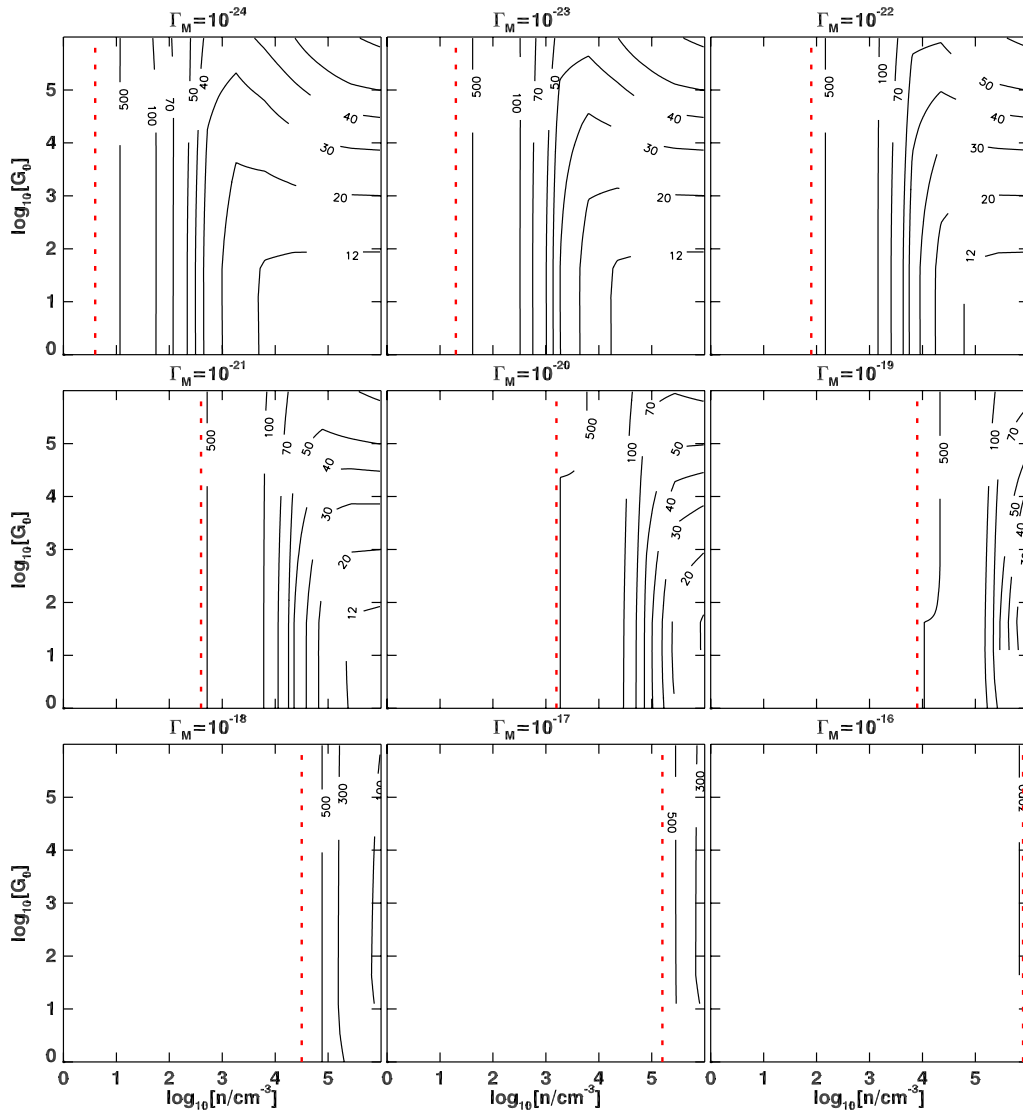
Appendix A

Fig. A.1. Temperature contours at $A_V = 20$ for different values of mechanical heating. As mechanical heating is increased from 10^{-24} to 10^{-16}, the temperatures increase *from left to right* in the grid as function of increasing mechanical heating. The temperatures to the left of the highest temperature contour line are higher than the temperature of the contour curve itself, which are usually larger than 10 000 K. The models in these regions are not very accurate since cooling effects for temperature larger than 10 000 K are not included properly, so we do not plot the corresponding contours.
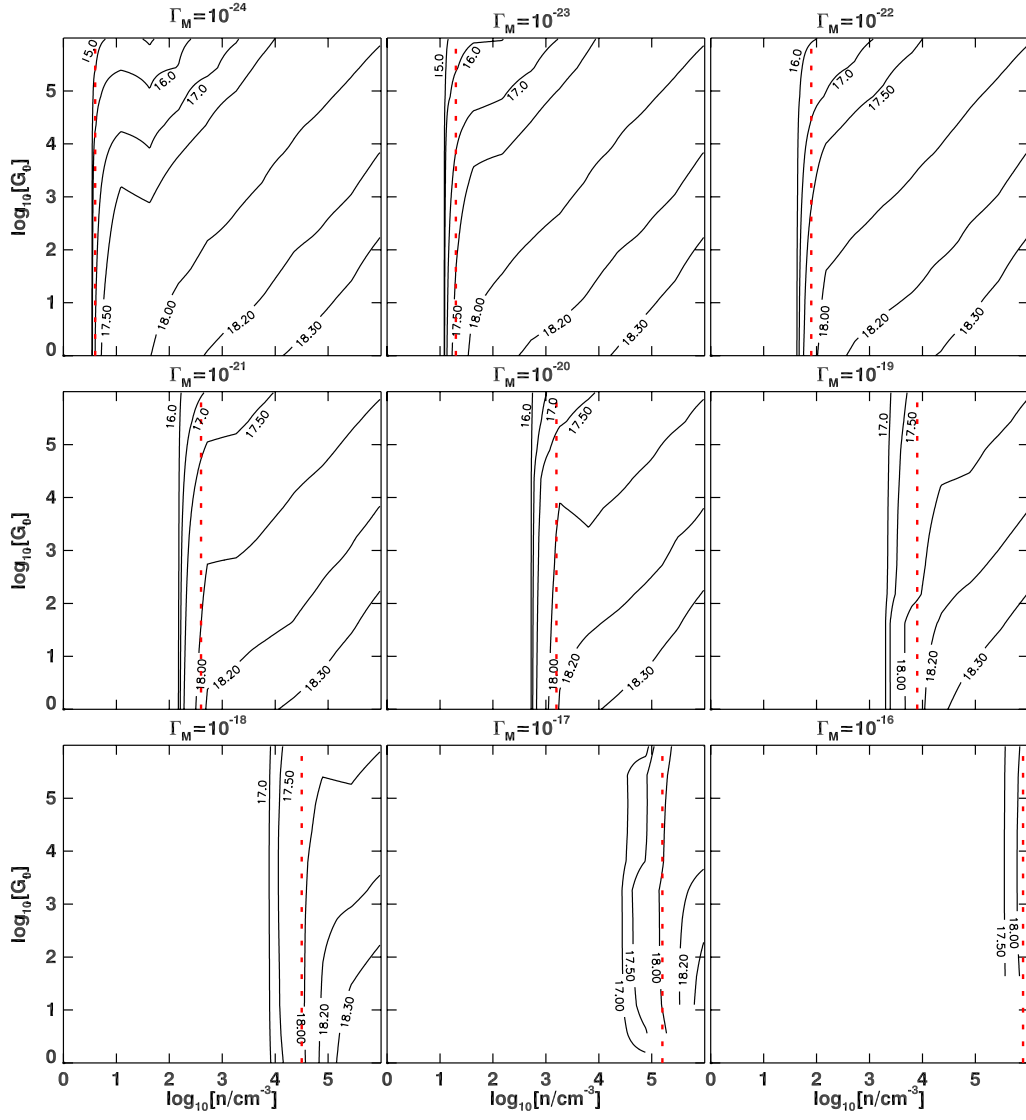
Fig. A.2. $\log_{10}$ CO total column density (integrated up to $N(\mathrm{H}) = 1.8 \times 10^{22}$ cm^{-2} or $A_V \sim 10$ mag for $Z = Z_\odot$) for different values of mechanical heating.
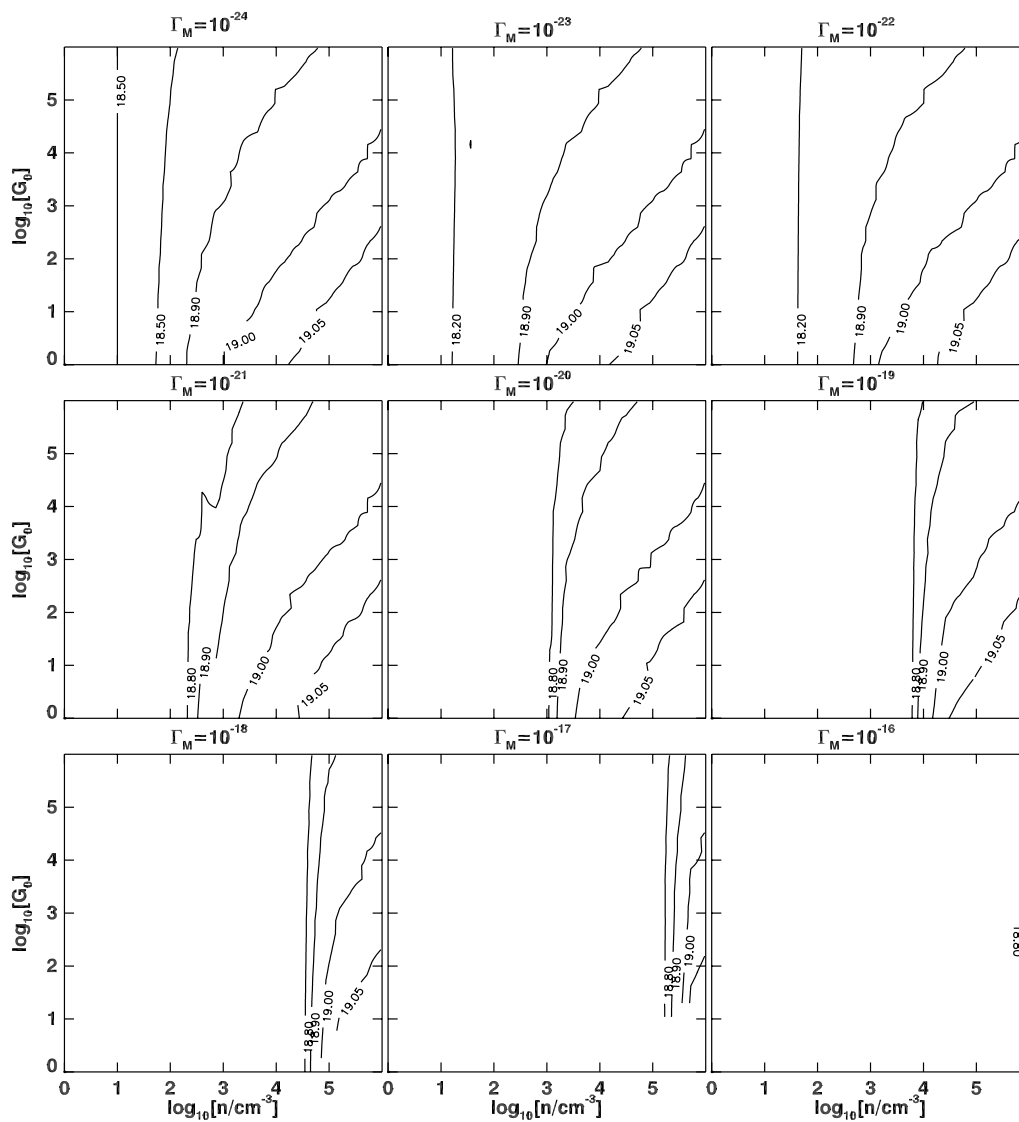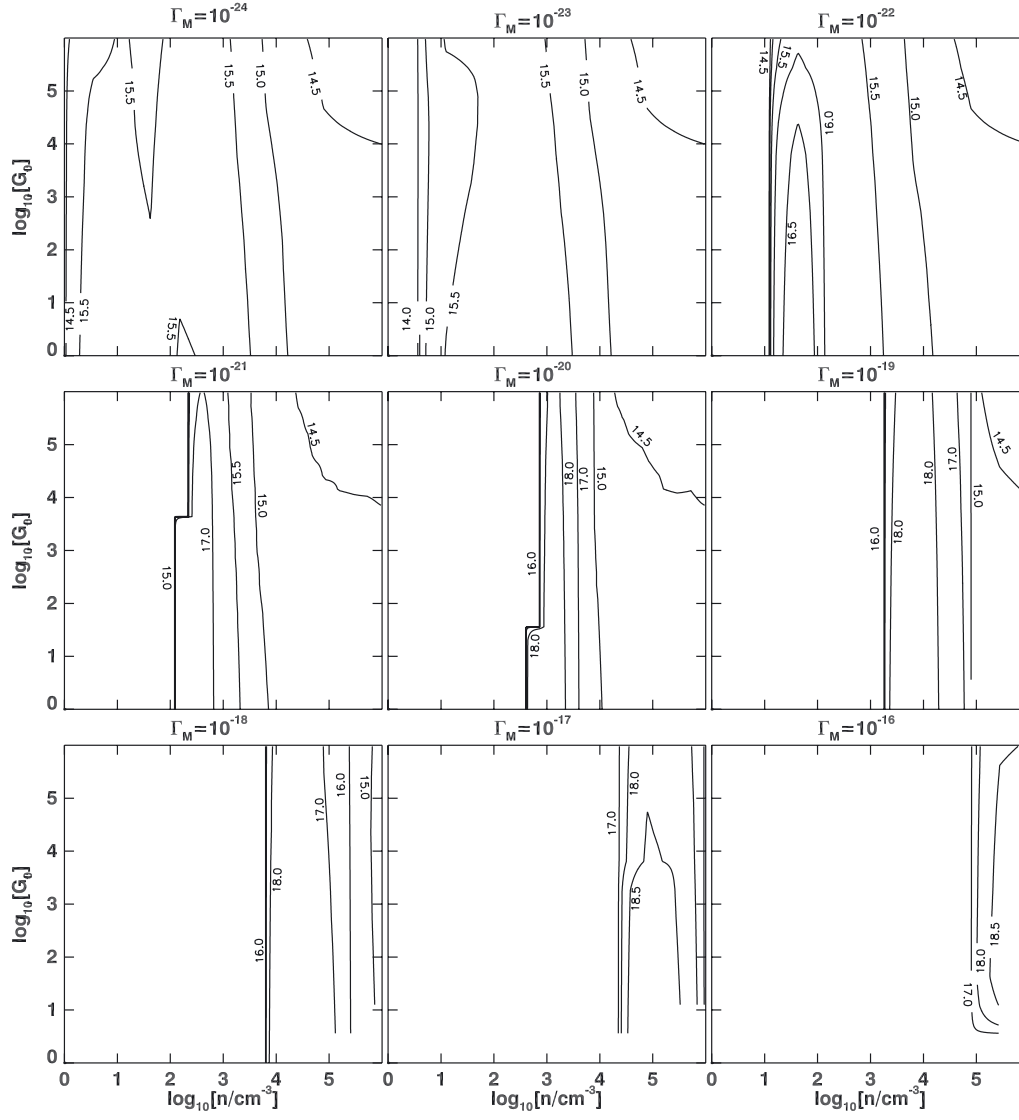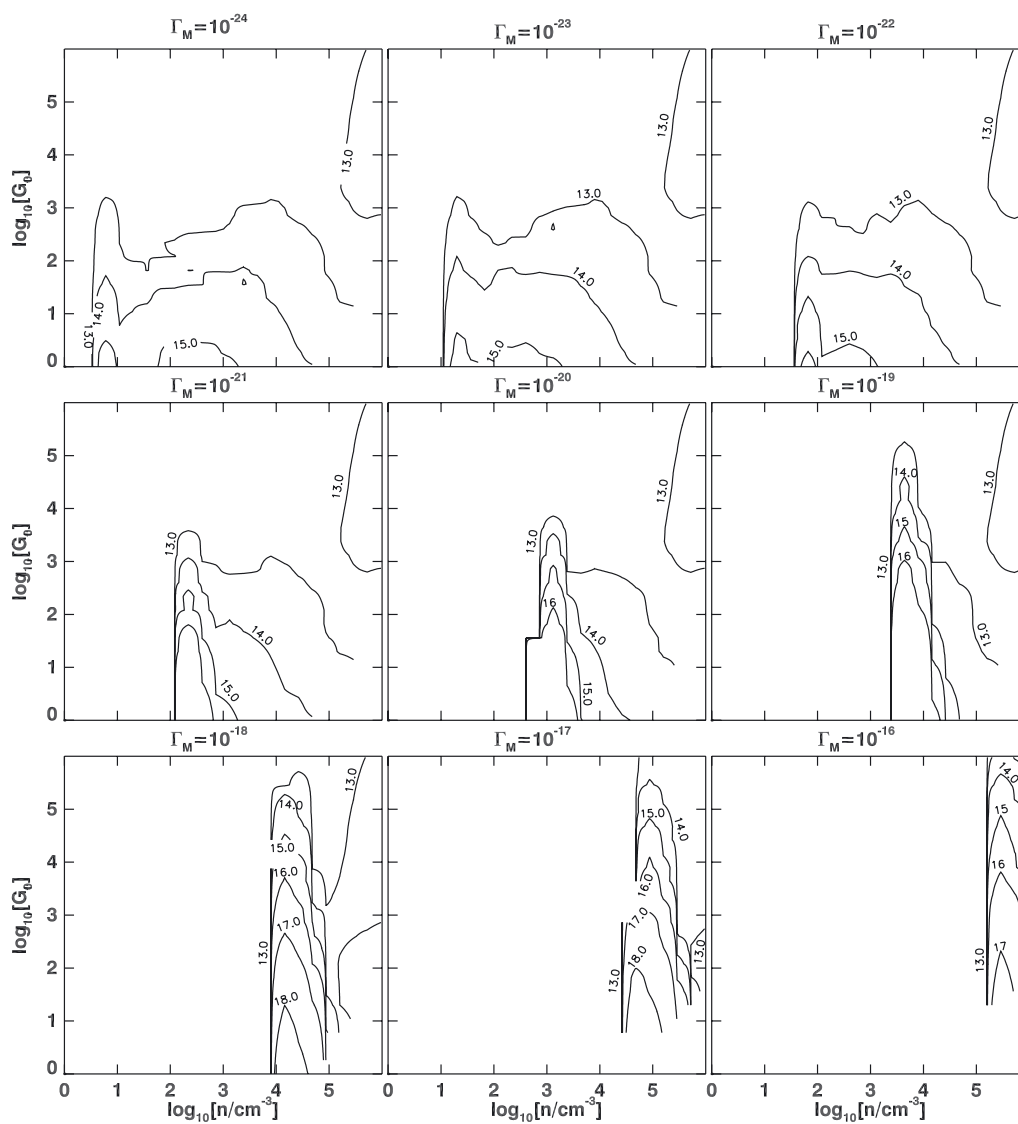
Fig. A.3. $\log_{10}$ CO total column density (integrated up to $N(\mathrm{H}) = 1.8 \times 10^{22}$ cm^{-2} or $A_{\mathrm{V}} \sim 20$ mag for $Z = 2\,Z_{\odot}$) as a function of mechanical heating for the double solar metallicity case.
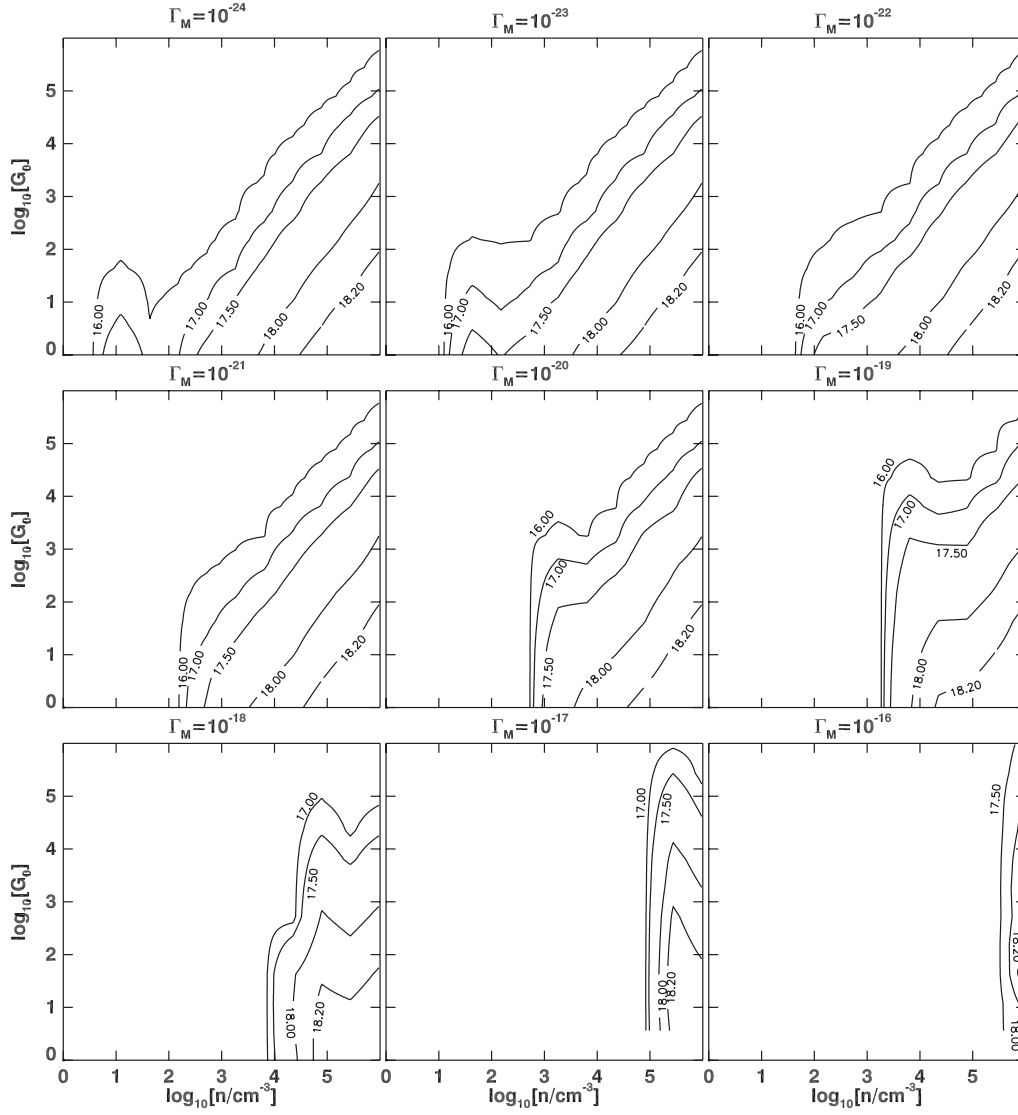
Fig. A.4. $\log_{10}$ CO total column density (integrated up to $N(\mathrm{H}) = 1.8 \times 10^{22}$ cm^{-2} or $A_V \sim 5$ mag for $Z = 0.5\ Z_\odot$) as a function of mechanical heating for the low metallicity case.
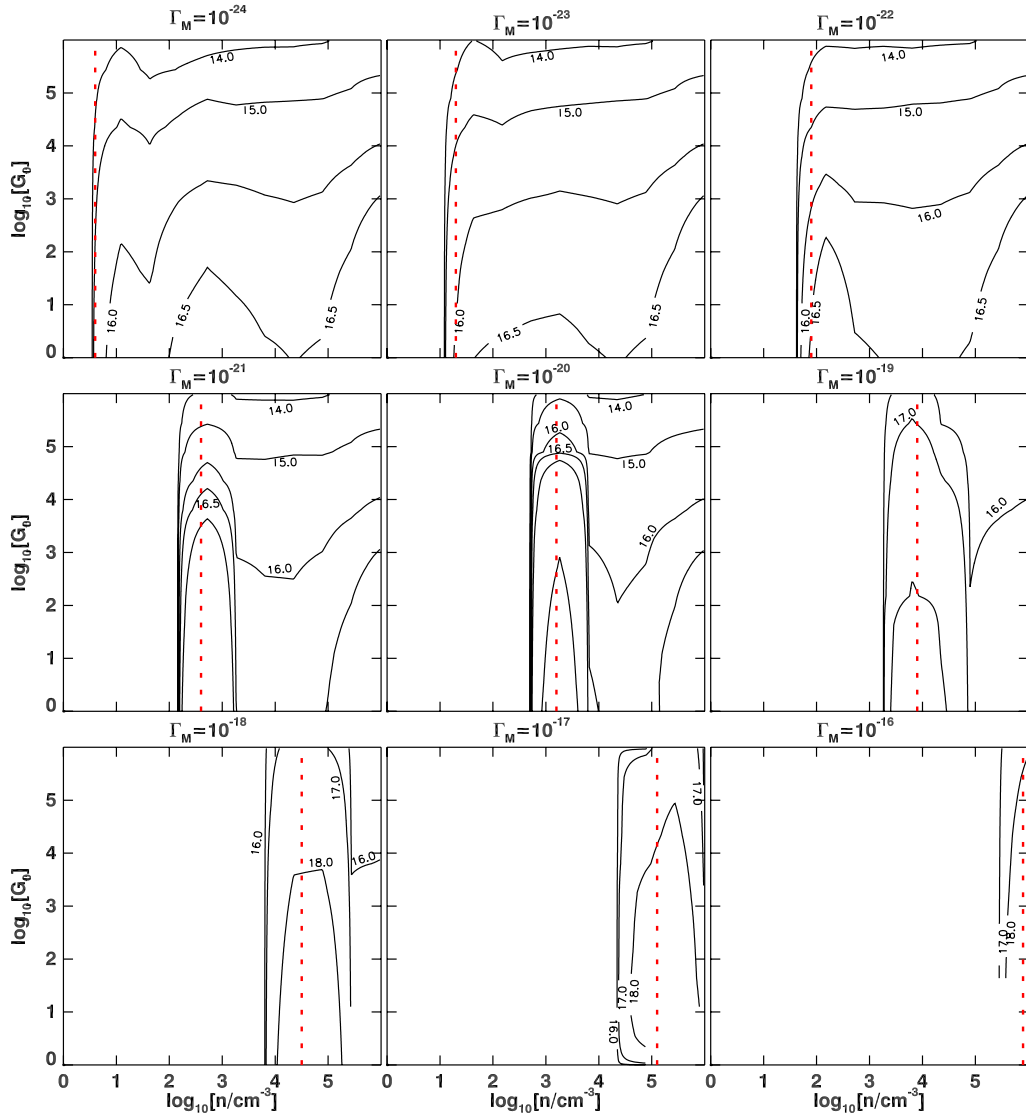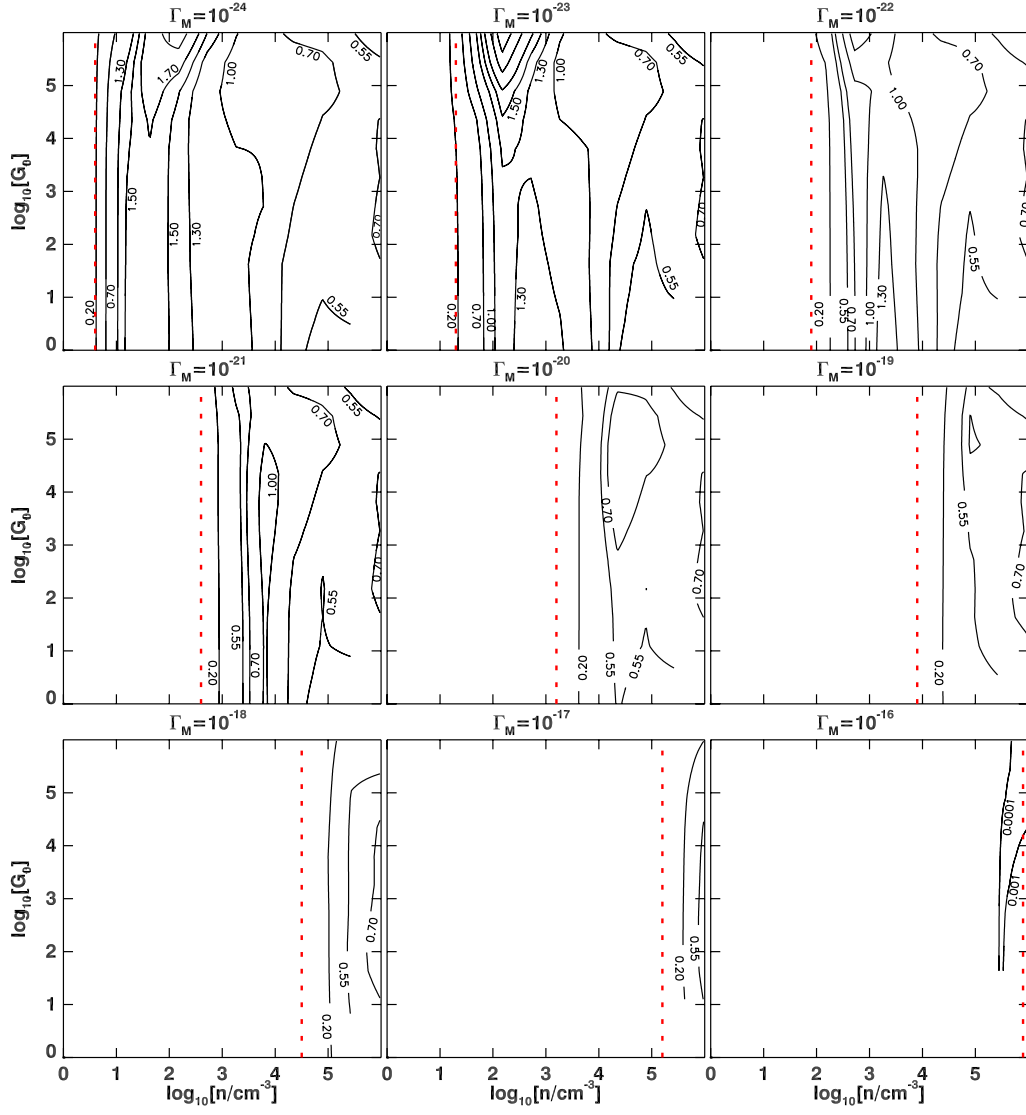
Fig. A.5. $\log_{10}$ H_2O total column density (integrated up to $N(H) = 1.8 \times 10^{22}$ cm^{-2} or $A_V \sim 10$ mag for $Z = Z_\odot$) for different values of mechanical heating.

Fig. A.6. $\log_{10}$ H$_2$O total column density (integrated up to $N(\mathrm{H}) = 1.8 \times 10^{22}$ cm^{-2} or $A_\mathrm{V} \sim 20$ mag for $Z = 2\,Z_\odot$) as a function of mechanical heating for the double solar metallicity case.
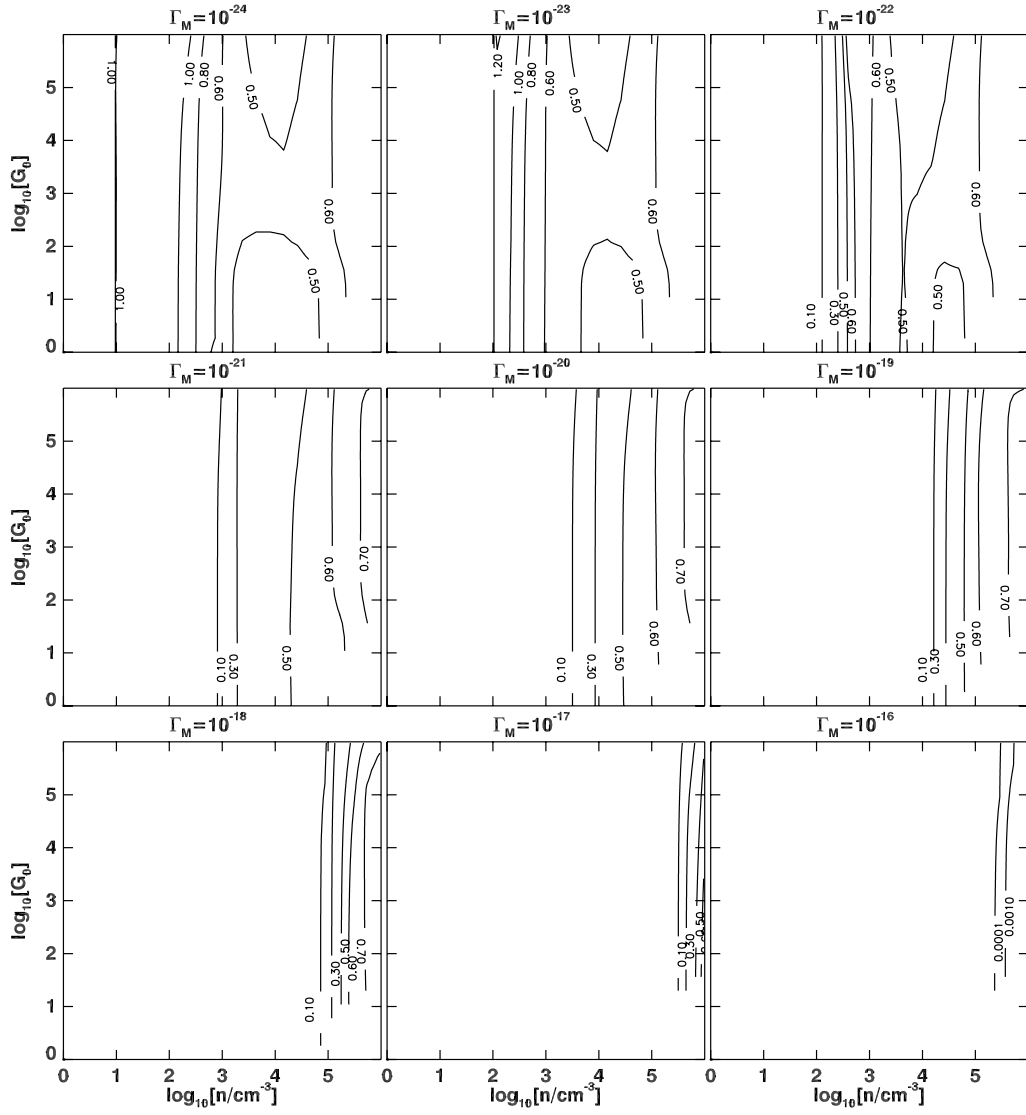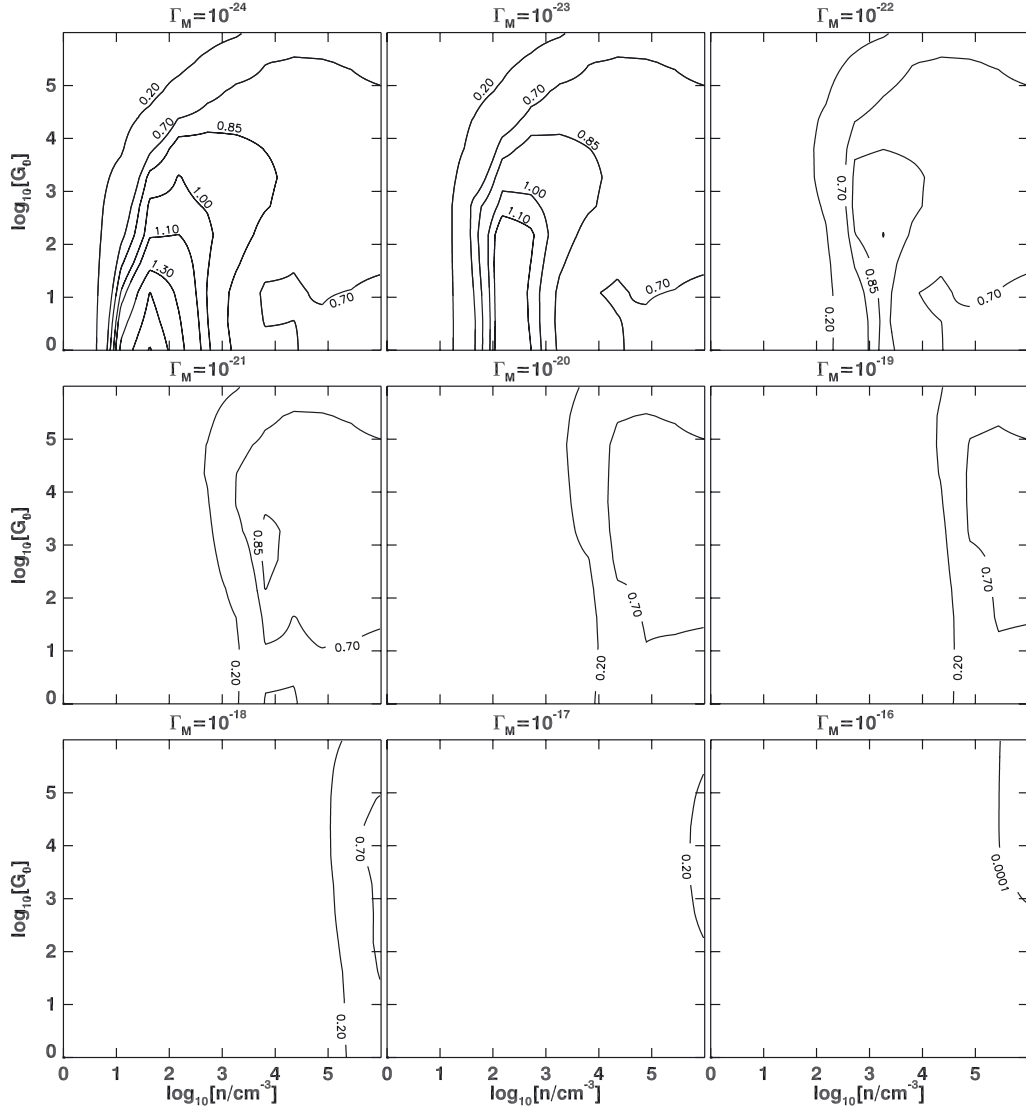
Fig. A.7. $\log_{10}$ H_2O total column density (integrated up to $N(H) = 1.8 \times 10^{22}$ cm^{-2} or $A_V \sim 5$ mag for $Z = 0.5$ $Z_\odot$) as a function of mechanical heating for the low metallicity case.

Fig. A.8. HNC/HCN integrated column density ratios (integrated up to $N(H) = 1.8 \times 10^{22}$ cm^{-2} or $A_V \sim 10$ mag for $Z = Z_\odot$) as a function of mechanical heating.

Fig. A.9. HNC/HCN column density ratios (integrated up to $N(\text{H}) = 1.8 \times 10^{22}$ cm^{-2} or $A_\text{V} \sim 20$ mag for $Z = 2\ Z_\odot$) as a function of mechanical heating for the double solar metallicity case.

Fig. A.10. HNC/HCN integrated column density ratios (integrated up to $N(H) = 1.8 \times 10^{22}$ cm^{-2} or $A_V \sim 5$ mag for $Z = 0.5\ Z_\odot$) as a function of mechanical heating for the low metallicity case.

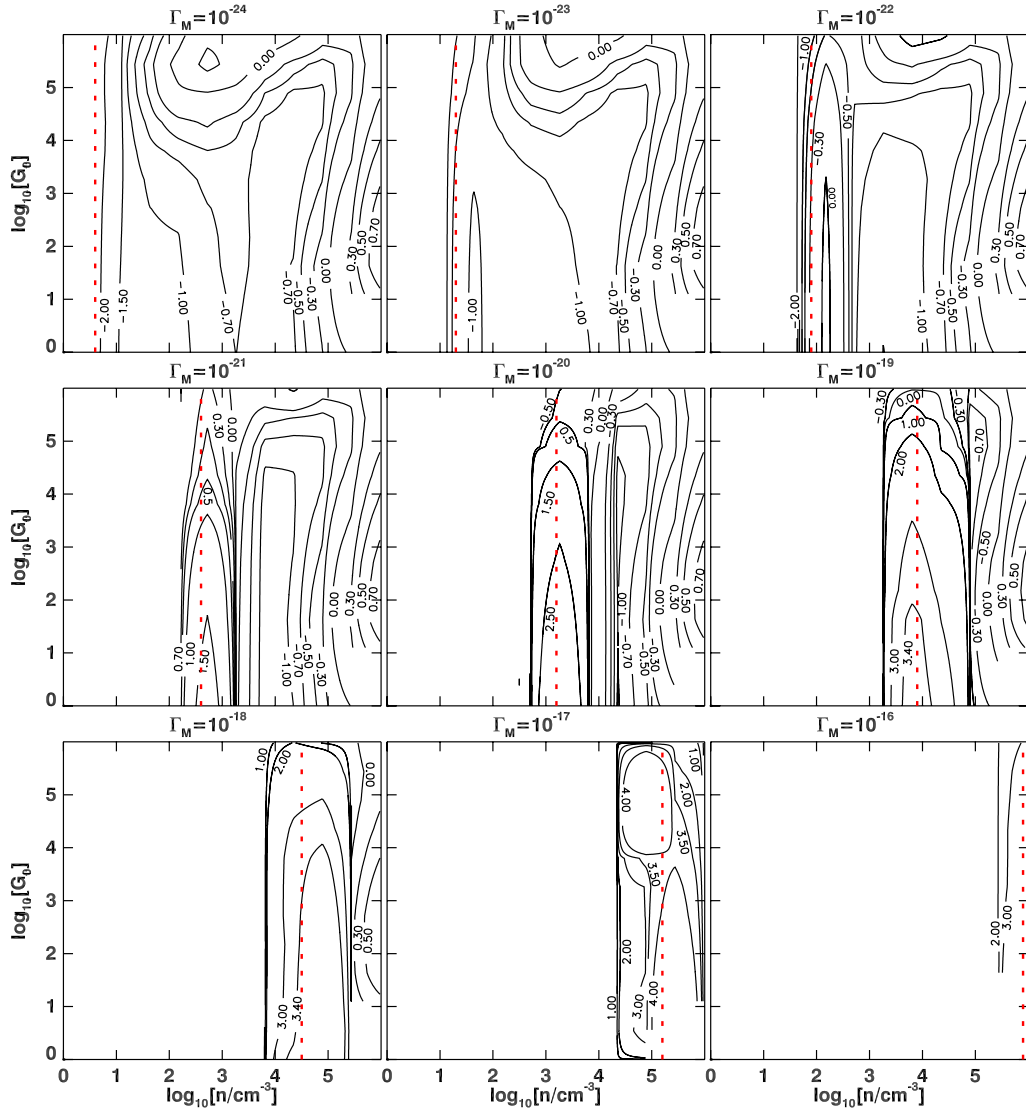**Fig. A.11.** $\log_{10}$ HCN/HCO$^+$ integrated column density ratios (integrated up to $N(\mathrm{H}) = 1.8 \times 10^{22}$ cm^{-2} or $A_\mathrm{V} \sim 10$ mag for $Z = Z_\odot$) as a function of mechanical heating for solar metallicity.
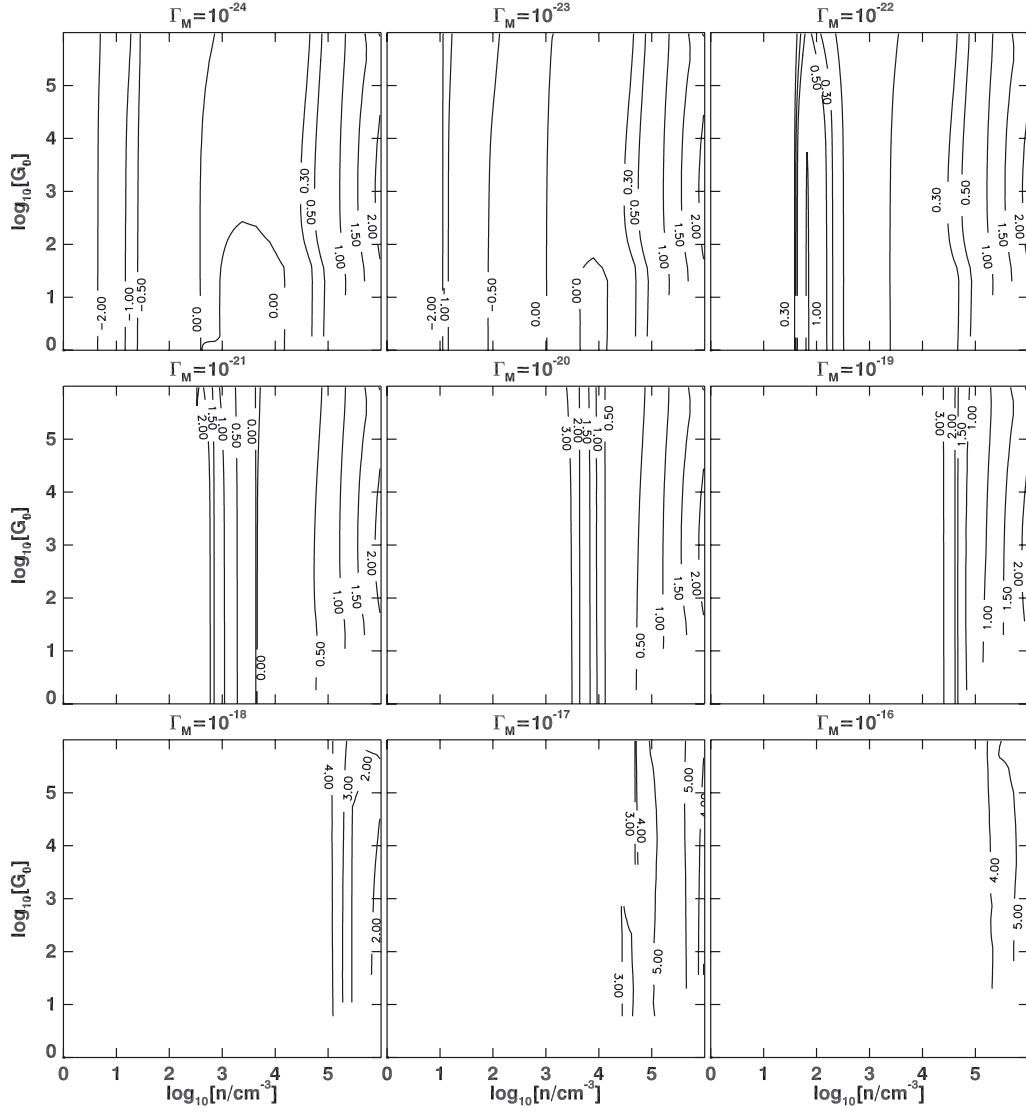
Fig. A.12. $\log_{10}$ HCN/HCO$^+$ column density ratios (integrated up to N(H) $= 1.8 \times 10^{22}$ cm^{-2} or $A_V \sim 20$ mag for $Z = 2\,Z_\odot$) as a function of mechanical heating for the double solar metallicity case.
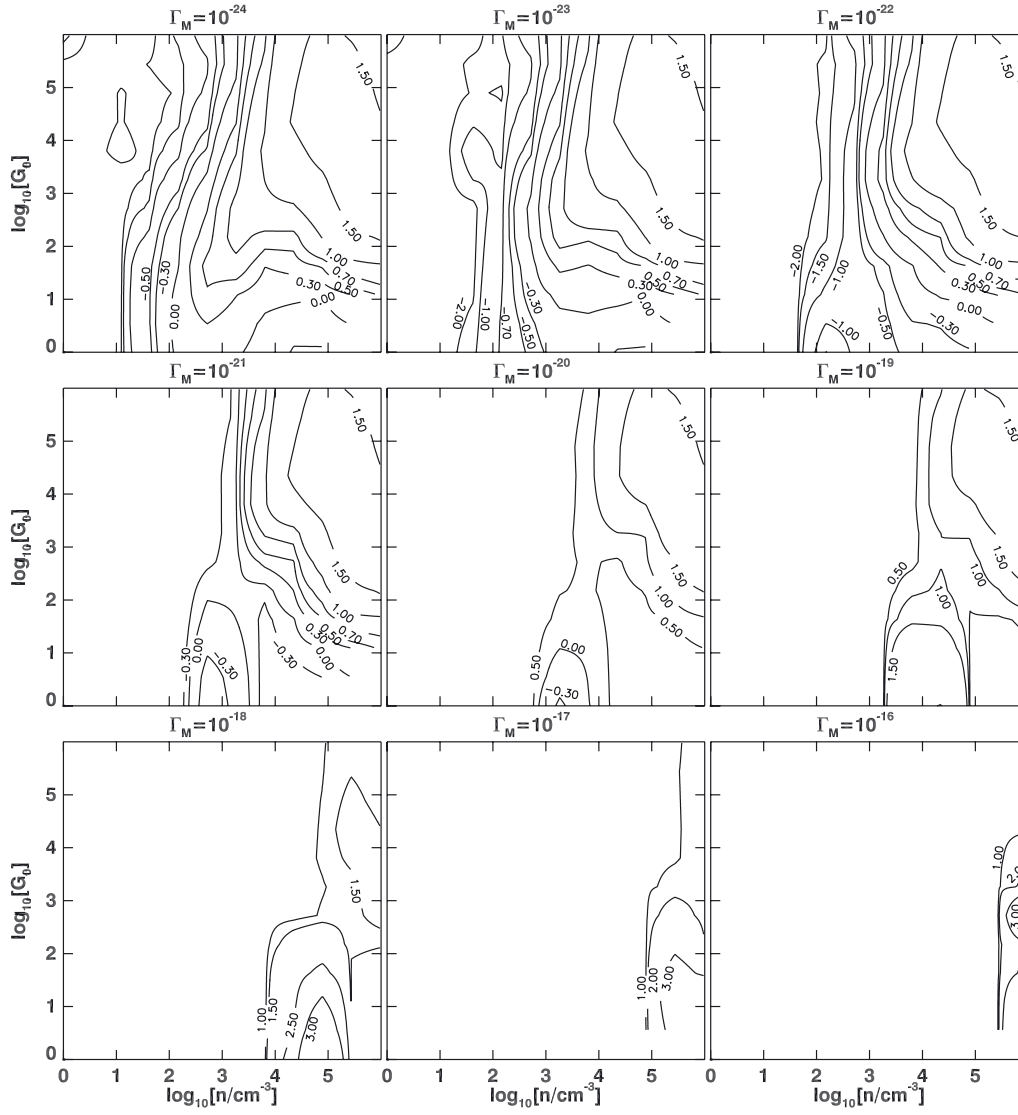
Fig. A.13. $\log_{10}$ HCN/HCO$^+$ integrated column density ratios (integrated up to $N(\mathrm{H}) = 1.8 \times 10^{22}$ cm^{-2} or $A_V \sim 5$ mag for $Z = 0.5\,Z_\odot$) as a function of mechanical heating for the low metallicity case.